Received: 15 September 2023 | Revised: 8 July 2024 | Accepted: 12 July 2024

DOI: 10.1111/bph.17305

RESEARCH ARTICLE

The PARP inhibitor rucaparib blocks SARS-CoV-2 virus binding to cells and the immune reaction in models of COVID-19

Henrietta Papp[1,2,3] | Emese Tóth[4,5] | Judit Bóvári-Biri[3,6] | Krisztina Bánfai[3,6] | Péter Juhász[7] | Mohamed Mahdi[8] | Lilian Cristina Russo[9] | Dávid Bajusz[10] | Adrienn Sipos[4,5] | László Petri[10] | Tibor Viktor Szalai[10,11] | Ágnes Kemény[3,12,13] | Mónika Madai[1,2,3] | Anett Kuczmog[1,2,3] | Gyula Batta[14] | Orsolya Mózner[15,16] | Dorottya Vaskó[17] | Edit Hirsch[17] | Péter Bohus[18] | Gábor Méhes[7] | József Tőzsér[8] | Nicola J. Curtin[19] | Zsuzsanna Helyes[12,20,21] | Attila Tóth[22] | Nicolas C. Hoch[9] | Ferenc Jakab[1,2†] | György M. Keserű[10,17] | Judit E. Pongrácz[3,6] | Péter Bai[3,4,23,24]

Correspondence
Peter Bai, Faculty of Medicine, Department of Medical Chemistry, University of Debrecen, Egyetem tér 1., 4032 Debrecen, Hungary.
Email: baip@med.unideb.hu

Funding information
Fundação de Amparo à Pesquisa do Estado de São Paulo, Grant/Award Numbers: 2018/18007-5, 2020/05317-6; Nemzeti Kutatási Fejlesztési és Innovációs Hivatal, Grant/Award Numbers: FK146852, K132623, K135150, K142141, PD142301, RRF-2.3.1-21-2022-00010, SNN135335, TKP-2021-EGA-13, TKP2021-EGA-10, TKP2021-EGA-19, TKP2021-EGA-20, TKP2021-NVA-07, UNKP- 21-5, FK146063, 2020-1.1.2-PIACI-KFI-2020-00039; Magyar Tudományos Akadémia, Grant/Award Number: POST-COVID2021-33

Abstract

Background and Purpose: To date, there are limited options for severe Coronavirus disease 2019 (COVID-19), caused by SARS-CoV-2 virus. As ADP-ribosylation events are involved in regulating the life cycle of coronaviruses and the inflammatory reactions of the host; we have, here, assessed the repurposing of registered PARP inhibitors for the treatment of COVID-19.

Experimental Approach: The effects of PARP inhibitors on virus uptake were assessed in cell-based experiments using multiple variants of SARS-CoV-2. The binding of rucaparib to spike protein was tested by molecular modelling and microcalorimetry. The anti-inflammatory properties of rucaparib were demonstrated in cell-based models upon challenging with recombinant spike protein or SARS-CoV-2 RNA vaccine.

Key Results: We detected high levels of oxidative stress and strong PARylation in all cell types in the lungs of COVID-19 patients, both of which negatively correlated with lymphocytopaenia. Interestingly, rucaparib, unlike other tested PARP inhibitors, reduced the SARS-CoV-2 infection rate through binding to the conserved 493–498 amino acid region located in the spike-ACE2 interface in the spike protein and prevented viruses from binding to ACE2. In addition, the spike protein and viral RNA-

Abbreviations: ACE2, angiotensin-converting enzyme 2; ARDS, acute respiratory distress syndrome; COPD, chronic obstructive pulmonary disease; COVID-19, Coronavirus disease 2019; ELISA, enzyme-linked immunosorbent assay; FFPR, formalin-fixed, paraffin embedded; HRP, horseradish peroxidase; H6PD, hexose-6-phosphate dehydrogenase; ITC, isothermal titration calorimetry; LPS, lipopolysaccharide; PAR, poly(ADP-ribose); PARylation, poly(ADP-ribosyl)ation; RBD, receptor-binding domain of spike; PBMC, peripheral blood mononuclear cells; PEI, polyethylenimine; PS, penicillin–streptomycin; STD-NMR, saturation difference spectrum NMR; TBST, Tris buffered saline + 0.05% Tween-20; TMB, 3,3′,5,5′-tetramethylbenzidine; 4HNE, 4-hydroxynonenal.

Henrietta Papp, Emese Tóth, Judit Bóvári-Biri and Krisztina Bánfai have equal contributions.

† Died 16th February 2024.

For affiliations refer to page 4799

induced overexpression of cytokines was down-regulated by the inhibition of PARP1 by rucaparib at pharmacologically relevant concentrations.

Conclusion and Implications: These results point towards repurposing rucaparib for treating inflammatory responses in COVID-19.

KEYWORDS

ACE2, COVID-19, NFκB, rucaparib, SARS-CoV-2 RNA, SARS-COV-2 spike protein, viral lung inflammation

1 | INTRODUCTION

Coronavirus disease 2019 (COVID-19), caused by SARS-CoV-2 virus infection, is a global health challenge. SARS-CoV-2 is an enveloped virus with an ssRNA+ genome belonging to the *Coronaviridae* family (Gorbalenya et al., 2020). SARS-CoV-2 predominantly infects the upper airways that may then transfer to lower airways causing atypical lung inflammation (Zhu et al., 2020). The virus uses the **angiotensin-converting enzyme 2** (ACE2) as a cellular receptor for entry into epithelial cells (Hoffmann et al., 2020). Although 80% of the patients develop mild or no symptoms, 15% develop severe disease requiring oxygen support, and 5% develop critical illness. The inflammatory response during the disease strongly contributes to organ damage and critical illness (Fu et al., 2020) in which **Interleukin-6** (IL-6) has a pivotal role (McElvaney et al., 2020). Severe COVID-19 remains an unmet medical need calling for novel therapeutic modalities. For that reason, we set out to investigate clinically approved **PARP** inhibitors.

PARPs are ADP-ribosyl transferase enzymes composed of 17 members in humans (PARP1–PARP16) (Lüscher et al., 2022). **PARP1**, **PARP2**, **TNKS1** and **TNKS2** can generate poly(ADP-ribose) (PAR) chains, while other members of the family, with the exception of PARP13, can attach one (mono-ADP-ribosylation) or a few ADP-ribose units (oligo-ADP-ribosylation) to target proteins (Lüscher et al., 2022). PARP1, PARP2 and **PARP3** can be activated by damaged DNA (Lüscher et al., 2022) that is often the result of reactive oxygen species (ROS) that are produced under inflammatory conditions (Bai & Virag, 2012). PARP activation contributes to necrotic and apoptotic cell death (Curtin et al., 2020). Furthermore, PARP activation has proinflammatory properties (Bai & Virag, 2012; Curtin & Szabo, 2020; Morrow et al., 2009). Four small molecule pharmacological PARP inhibitors, **olaparib**, **rucaparib**, **niraparib** and **talazoparib** are FDA/EMA-approved for cancer therapy, and fluzoparib and **pamiparib** are approved by the Chinese NMPA (Curtin & Szabo, 2020).

In models of COVID-19, oxidative stress (Abouhashem et al., 2020; Fodor et al., 2021; Karu et al., 2022; Montiel et al., 2022; Tangos et al., 2022) and PARylation have been reported (Heer et al., 2020). These processes may have a multi-pronged feed-forward effect on SARS-CoV-2 infection and COVID-19 disease including effects on virus replication, cell death and tissue injury or inflammatory processes (see Curtin et al., 2020). Therefore, PARP inhibition may have a multi-pronged pharmacological effect in COVID-19 disease, by blocking both SARS-CoV-2 replication and suppressing the consequent immune reaction. In fact, a recent report suggested that stenoparib, a PARP inhibitor of both classical PARPs and tankyrases, can block the replication of SARS-CoV-2 (Zarn et al., 2022). Based on these findings, we investigated the opportunity for repurposing registered pharmacological PARP inhibitors for the treatment of COVID-19.

What is already known

- ADP-ribosylation increases during the life cycle of coronaviruses and upon viral infection-induced inflammation.
- We hypothesise therefore that PARP inhibitors, such as rucaparib, could be repurposed to treat COVID-19.

What does this study add

- In cell cultures, rucaparib blocks SARS-CoV-2 binding to ACE2 through binding to the spike protein.
- Rucaparib decreased spike protein and virus RNA-induced cytokine release.

What is the clinical significance

- Rucaparib could be repurposed as an anti-inflammatory drug in COVID-19.

2 | METHODS

2.1 | Statements on chemicals and experimentation

Rucaparib was a generous gift from Dr. Thomas Harding (Clovis Oncology, Boulder, CO, USA). All routine chemicals were obtained from Sigma (St. Louis, MO, USA) unless stated otherwise. The source and RRIDs of all key chemicals, kits and primers are provided in Table S1. In plate-based assays, plate layout was varied among repeated experiments.

2.2 | Tissues from patients with COVID-19

This study was authorized by the local ethical board (6043/2022). Formalin-fixed, paraffin embedded (FFPE) blocks from patients who died of COVID-19 at Szent Erzsébet Hospital (Sátoraljaújhely, Hungary) between 30th November 2020 and 6th February 2021 were assessed. Controls were patients who died of non-COVID-19 causes during the same period at the clinical units of the University of Debrecen. We excluded patients with nosocomial infections in their records. Patient data was accessed and the haemogram values closest to the time of death was used for statistics. Demographics of the patients are shown in Table S2.

2.3 | Blood donors

Monocytes were prepared from buffy coat of healthy donors. The study was authorized by the local ethical board (Reg. No. 938-2/2014/5200). Three-three donors were used in the LPS-induction and spike-induction experiments. Informed consent was obtained from all participants.

2.4 | Immunohistochemistry for poly(ADP-ribose), 4-hydroxynonenal and spike protein

Five-micron thick sections were obtained from formalin-fixed, paraffin-embedded blocks of COVID-19 patients and controls. Tissues were formalin-fixed 24 h after excision. Immunohistochemistry was performed, as described by Csonka et al. (2014), with the conditions in Table S3. Scoring was performed without knowledge of the cell treatments. We scored the intensity of spike protein immunostaining (0–3), counted the proportion of cells positive for 4-hydroxynonenal (4HNE) (0%–100%), scored the intensity of poly(ADP-ribose) (PAR) immunostaining (0–3) and counted the per cent of PAR-positive cells (0%–100%). The two pathologists evaluated the staining independently, the evaluations were subsequently discussed and an agreed score was generated.

For the evaluation of immunohistochemistry, a Leica DM2500 light microscope was used at a magnification of 20× (aperture 0.4) and 40× (aperture 0.65) at room temperature without the use of immersion oil. For the acquisition of images, a Leica Microsystems Ltd. model: DFC495 (12730471) camera was used. Images were captured using the LAS V4.13 software from Leica.

2.5 | Cell culture

Vero E6 cells were cultured at 37°C, 5% CO_2 in DMEM supplemented with 10% FBS and 1% penicillin–streptomycin (PS).

Human embryonic kidney cells (HEK-293T) cells expressing ACE2 receptor and the **TMPRSS2** protease (GeneCopoeia, Rockville, MD, USA) were grown in DMEM supplemented with 10% FBS and selection antibiotics (hygromycin 100 $\mu g \cdot ml^{-1}$, puromycin 1 $\mu g \cdot ml^{-1}$) and maintained in 37 C, 5% CO_2 incubator.

A549 lung adenocarcinoma constitutively expressing FLAG-tagged SARS-CoV-2 **Nsp3** macrodomain or its control empty vector (Russo et al., 2021) were grown in DMEM/high glucose media (Thermo) supplemented with 10% fetal bovine serum (Thermo) and maintained at 37°C in a humidified atmosphere containing 5% CO_2. Rucaparib does not modify the expression of the macrodomain transgene (Figure S2).

Human pulmonary alveolar epithelial cells (HPAEpiC) were purchased from Innoprot Inc. (cat. no. P10556, Derio, Spain) and cultured at 37°C in a humidified atmosphere containing 5% CO_2. Cells were grown in alveolar epithelial cell medium supplemented with 10% fetal bovine serum, 1% epithelial cell growth supplement and 1% penicillin/streptomycin solution, each included in Alveolar Epithelial Cell Medium Kit (cat. no. P60102, Innoprot Inc., Derio, Spain, P60102). Cell culture flasks for HPAEpiC cells were coated with 2 $\mu g \cdot cm^{-2}$ poly-L-lysine (cat. no. PLL, Innoprot Inc., Derio, Spain). All cells were confirmed mycoplasma free by PCR analysis and were regularly tested during the experiments.

2.6 | Viruses

SARS-CoV-2 B.1.5 (Accession ID: EPI_ISL_483637, with D614G mutation; Korber et al., 2020) and B.1.1.7. (Accession ID: EPI_ISL_826270) variants were isolated at the National Laboratory of Virology (University of Pécs, Pécs, Hungary). Variants were verified by sequencing.

SARS-CoV-2 spike protein-pseudotyped lentivirions were produced by transfection of HEK-293T cells with the following plasmids: pLenti CMV GFP Puro expression vector, psPAX2 packaging plasmid (Addgene, Watertown, MA, USA) and pcDNA3.1 plasmids coding for either the Wuhan-Hu-1 prototypical, the 1.617 or the 1.351 SARS-CoV-2 spike variant (GenScript Biotech, Piscataway NJ, USA). Transfection was done in a 1:1:1 ratio using the polyethylenimine (PEI) method, and virion production was carried out as described previously (Mahdi et al., 2018). Following collection and concentration of the pseudovirions, an enzyme-linked immunosorbent assay (ELISA)-based colorimetric reverse transcriptase (RT) assay (Roche Applied Science, Mannheim, Germany) was then used to detect the amount of RT in the virus samples, and transduction (infection) of cells was carried out using 4-ng RT-equivalent of the pseudovirions (MOI 0.2).

All viruses were handled in labs with the required biosafety.

2.7 | Virus proliferation assay

In a 96-well cell culture plate, 3×10^5 Vero E6 cells were seeded 1 day prior to infection. Treatment with the different PARP inhibitors (rucaparib, olaparib, talazoparib) from 40 to 2.5 μM commenced simultaneously with the infection of SARS-CoV-2 (Accession ID: EPI_ISL_483637, B.1.5 variant) at MOI 0.01 in a BSL-4 laboratory. After a 30-min incubation at 37°C in an atmosphere of 5% CO_2 in

air, the mixture was replaced with culture medium containing the PARP inhibitor; 48 h post-infection, the supernatant was collected. RNA extraction was performed using the Monarch Total RNA miniprep kit (New England Biolabs, Ipswitch, MD, USA). Viral titre from the supernatant was determined using a QX200 AutoDG Droplet- Digital PCR using the ddPCR Supermix (both from Bio-Rad, Hercules, CA, USA). The PCR was specific for the SARS-CoV-2 RdRp gene (forward primer: GTGARATGGTCATGTGTGGCGG; reverse: CARATGTTAAASACACTATTAGCATA, probe FAM-CAGGTGGA-ACCTCATCAGGAGATGC-BBQ). IC_{50} was determined by performing a non-linear regression using the [Inhibitor] vs. response variable slope (four parameters) macro of GraphPad Prism. For rucaparib, the R^2 value was $R^2_{infection} = 0.8176$.

2.8 | Viability assays

Cell viability was assessed in Vero E6 cells using the CellTiter-Glo assay (Promega, Madison, WI, USA). IC_{50} was determined by performing a non-linear regression using the [Inhibitor] versus response variable slope (four parameters) macro of GraphPad Prism. The R^2 value for the goodness of fit was $R^2_{viability} = 0.9776$ for Rucaparib.

2.9 | Neutralization assay on Vero E6 cells

A total of 8×10^5 Vero E6 cells were seeded in a 48-well plate. The next day, the plate was transferred to the BSL-4 laboratory. SARS-CoV-2 B.1.1.7 viral stocks were diluted to 0.01 MOI in DMEM (Lonza, Basel, Switzerland). Virus suspension (25 µl) was mixed with 25-µl rucaparib (60, 44 and 10 µM diluted in DMEM) and incubated for an hour at room temperature. After the incubation period, 450-µl DMEM was added to the mixture, which was then added to the cells. The cells were infected for 30 min at 37°C. The SARS-CoV-2 and rucaparib mixture was then discarded, and the cells were incubated for 2 days with drug and virus-free DMEM supplemented with 2% FBS and 1% Pen-Strep; 48 h post-infection, the supernatant was collected. RNA extraction was performed using the EXM 3000 nucleic acid isolation system (Zybio, Chongqing, China). Viral titre from the supernatant was determined using a QX200 AutoDG Droplet- Digital PCR using the ddPCR Supermix (both from Bio-Rad, Hercules, CA, USA). The PCR was specific for the SARS-CoV-2 RdRp gene (forward primer: GTGARATGGT-CATGTGTGGCGG; reverse: CARATGTTAAASACACTATTAGCATA, probe FAM-CAGGTGGAACCTCATCAGGAGATGC-BBQ).

2.10 | Neutralization assay on hybrid HEK293T cells

The day before the experiment, HEK-293T cells expressing ACE2 receptor and the TMPRSS2 protease (GeneCopoeia, Rockville, MD, USA) were seeded into 48-well plate (30,000 cells per well) in complete DMEM containing 10% FBS and 1% **penicillin–streptomycin**. On the next day, 35 µM of rucaparib in DMSO was incubated with 4 $ng \cdot \mu l^{-1}$ RT-equivalent of the pseudovirions for 30 min in DMEM medium without serum or antibiotics (50 µl total), at 37°C. For controls, equivalent amount of DMSO (0.7%) was added to the pseudovirions in the absence of rucaparib. The virus-containing medium was replaced with drug and virus-free complete DMEM medium. The cells were then incubated for 48 h in 37°C; after which, the media was removed from the wells, and the cells were collected in phosphate-buffered saline (PBS) (400 µl) for analysis of GFP fluorescence indicating transduction using flow cytometry (FACSCalibur, BD Bioscience, Franklin Lakes NJ, USA), counting 3000 cells per sample. Measurement was carried out in triplicates. Cells were visually inspected for signs of cell death, and signs of cell death were not observed in any of the experiments reported.

2.11 | Assessing the role of H6PD in SARS-CoV-2 infection

This set of experiments was performed similar to the neutralization assay experiments described above with the modifications as follows.

The day before transfection, HEK-293T cells expressing ACE2 and TMPRSS2 were passaged into a 48-well plate (35,000 cells per well) in DMEM containing 10% FBS and selection antibiotics. Cells were transfected with 15 pmol of a 1:1 mixture of s18370 (A) and s532906 (B) siRNAs using Lipofectamine transfection reagent according to the manufacturer's protocol.

After incubation for 24 h in 37°C 5% CO_2, the media was removed from the cells, 450 µl of fresh medium was added and transduction with the Wuhan-Hu-1 spike-pseudotyped lentivirions was carried out as described previously. Results were derived from triplicate measurements.

2.12 | Monocyte differentiation

Peripheral blood mononuclear cells (PBMC) were isolated from three different buffy coat samples received from the Hungarian National Blood Transfusion Service. To separate mononuclear cells, we layered the diluted blood sample in a 1:1 ratio with basal RPMI 1640 Medium (Lonza, Cat. No: 12-167F) onto the Lymphocyte Separation Medium 1077 (PromoCell, Cat. No: CC-44010.) and centrifuged at 400 x *g*, for 30 min, at room temperature with 4/1 acceleration/deceleration. The layer of the mononuclear cells was transferred, washed with PBS (Lonza, Belgium, Cat. No: 17-516F) and centrifuged at 300 x *g* for 10 min at room temperature. Following cell counting, 5×10^5 cells per well were seeded to 24-well plates (Greiner, Germany, Cat. No: 662160) in complete RPMI 1640 Medium supplemented with fetal bovine serum (Biosera, USA, MO, Cat. No: FB-1350-500), penicillin–streptomycin (Lonza, Belgium, Cat. No: DE17-602E) and **L-glutamine** (Lonza, Belgium, BE-17-605E). To induce macrophage differentiation, we incubated the cells for 5 days at 37°C, 5% CO_2 in a humidified atmosphere.

2.13 | Treatment of differentiated macrophages

In the first part of the experiment, differentiated macrophages were treated in three parallels/treatment group with combination of LPS and vehicle control 0.1% DMSO, 20-μM rucaparib, 20-μM olaparib, 10-μM talazoparib, 0.1-μM **dexamethasone** or 1-μM dexamethasone for 14 h. Following incubation, supernatants were collected for further investigation. Monocytes from three donors were accessed and were plotted.

In the second part of the experiment, differentiated macrophages from three different donors (30,000 cells per well) were pretreated for 48 h with 20-nM spike protein, and then rucaparib was added in five different concentrations (500 nM, 1 μM, 5 μM, 15 μM, 27 μM) and incubated for 24 h. Dexamethasone in 1 μM was used as a positive control. Supernatants and cell pellets were collected for further assays. One representative donor is displayed in three biological replicates due to a large heterogeneity of the donor responses.

2.14 | Inflammatory cytokine concentration measurement using Luminex xMAP technology

Luminex Multiplex Immunoassay was performed to determine the following cytokines/chemokine concentrations using customized Milliplex Human Cytokine/Chemokine/Growth Factor Panel A Magnetic Bead Panel (Cat. Nr. HCYTA-60 K, Merck Millipore, Darmstadt, Germany): **IL-10**; **IL-1β**; **IL-2**; **IL-6**; **IL-8**; **tumor necrosis factor-alpha** (TNF-α). Following previous optimizations, the undiluted samples were tested in a blind fashion and in duplicate. The experiment was performed according to the manufacturer's instructions. Briefly, 25-μl volume of each sample, control, and the standard was added to a 96-well plate (provided by the kit) containing 25 μl of fluorescent-coded, capture antibody-coated beads. After the appropriate washing and incubation periods, biotinylated detection antibodies and streptavidin-PE were added to the plate; 150-μl volume of drive fluid was added to the wells after the last washing step, and the plate was incubated and read on the Luminex MagPix instrument. Five-PL regression curves were used to plot the standard curves for the analytes by the Belysa 1.1 (Merck KGaA, Darmstadt, Germany) software analysing the bead median fluorescence intensity. Results are shown in picograms per milligram.

2.15 | Inflammatory cytokine concentration measurement using the Proquantum kit series

In spike induction experiments, IL-6 (A35575), TNFα (A35601) and IL-1β (A35574) were determined using the respective Proquantum assay kits (ThermoFisher, Waltham, MA, USA) according to the instructions of the manufacturer.

2.16 | Western blotting for the SARS-CoV-2 macrodomain experiments

Western blots were performed as previously described (Russo et al., 2021). For western blot, the seeding density was 2×10^5 cells per well. Cells were lysed directly in preheated boiling Laemmli buffer, quantified (BCA protein quantification kit, Pierce, Appleton WI, USA), loaded (20 μg) in standard 10% SDS-PAGE gels and transferred to nitrocellulose membranes (Bio-Rad, Hercules, CA, USA). Membranes were blocked with 5% skimmed milk for 30 min and incubated with primary antibodies (anti-p.STAT1—1:1000, Cell Signaling #9167; anti-FLAG—1:1000, Sigma #F1804; anti-tubulin—1:5000, Abcam #Ab18251) (Cell Signaling, Danves, MA, USA; Abcam, Cambridge, UK) diluted in 5% BSA in Tris-buffered saline with 0.05% Tween-20 (TBST) buffer, overnight at 4°C. Membranes were washed three times in TBST, incubated in appropriate HRP-conjugated secondary antibodies (Sigma), washed and incubated with ECL Prime (Amersham, Amersham, UK), and the signal was detected using a Chemidoc MP Imaging System (Bio-Rad, Hercules, CA, USA). Signals were quantified using ImageJ software.

2.17 | Immunofluorescence staining for ADP-ribose and FLAG

As previously described (Russo et al., 2021), A549 cells, either transduced with empty vector control or lentiviral constructs for FLAG-tagged SARS-CoV-2 macrodomain overexpression, were seeded in microscopy-compatible plastic 96-well plates at the density of 10^4 cells per well (Corning, Corning, NY, USA), treated as required, washed with PBS and fixed with 4% EM-grade PFA (EMS, Dormat, Switzerland), which was subsequently quenched twice with 0.1-M glycine and washed in PBS. After permeabilization in 0.2% TritonX-100 in PBS, samples were blocked in 10% FBS in permeabilization solution and incubated with primary antibodies (anti-ADP-ribose—1:500, Millipore #MABE1016; anti-FLAG—1:500, Sigma #F1804) (Millipore, Burlington MA, USA) for 1 h at room temperature in blocking solution. Samples were extensively washed in PBS, incubated with appropriate fluorescently labelled secondary antibodies (Thermo), stained with DAPI (Thermo), washed and maintained in 30% glycerol. The applied fluorochromes were DAPI, Alexa Fluor 488, Alexa Fluor 568 and Alexa Fluor 647 (Thermo), and the mounting medium was VectaShield (VectorLabs).

Fluorescence microscopy images were acquired on a customized TissueFAXS i-Fluo system (TissueGnostics, Wien, Austria) mounted on a Zeiss AxioObserver 7 microscope (Zeiss, Oberkochen, Germany), using Plan NeoFluar 2.5× (NA 0.075) and 20× Plan-Neofluar (NA 0.5) objective and an ORCA Flash 4.0 v3 camera (Hamamatsu, Hamamatsu city, Japan). Images were acquired at room temperature and processed and analysed using StrataQuest software (TissueGnostics, Wien, Austria). Several image processing operations were performed in order to detect subcellular structures (described in Russo

et al., 2021), but all signal quantifications were performed on minimally processed 16bit images.

All values were normalized to the IFNγ-treated empty vector control.

PAR immunofluorescence experiments were repeated eight times, while STAT1 phosphorylation or FLAG immunoblotting experiments were repeated four times. All values were normalized to the IFNγ-treated empty vector control.

2.18 | Immunofluorescence staining for pNFκB^{S276} detection

HPAEpiC (3×10^4) were seeded on poly-L-lysine (PLL, Innoprot Inc.) coated glass coverslips and pretreated with vehicle or rucaparib or IKK-16 and induced with SARS-CoV-2 Spike S1 protein or vaccine (Comirnaty Original/Omicron BA.1), as indicated in the figure legend. Samples were fixed with 4% PFA for 15 min and permeabilized with 0.2% Triton-X-100/PBS for 30 min. Between each step, cells were washed with PBS three times. Samples were blocked in 2% BSA/PBS for 1 h and then incubated with primary antibody (anti-RelA/NFκB pSer276 antibody, Novus Biologicals, cat.no. NB100–82086) for 1 h at room temperature in blocking solution. Cells were incubated with fluorescently labelled secondary antibody (Invitrogen, # A-21245) for 1 h at room temperature. Nuclei were stained with DAPI (NucBlue Fixed Cell Ready Probes Reagent, R37606, Invitrogen) for 5 min at room temperature in blocking solution.

Immunofluorescently labelled images were acquired using Leica TCS SP8 confocal microscope and LAS X 3.5.5.19976 software (Leica) using 63× oil immersion objective. Nonspecific binding of the secondary antibodies was tested in secondary antibody control experiments (data not shown).

The intensity of nuclear pNFκB^{S276} immunostaining was scored (0–3) by two blinded researchers. Difference between the nuclear score values was statistically tested using one-way ANOVA compared with vehicle-treated control cells.

2.19 | SARS-CoV-2 spike protein binding assay

Assessment of SARS-CoV2 RBD and hACE2 binding inhibition was performed using RayBio® COVID-19 spike-ACE2 binding assay kit (CoV-SACE2-1, RayBiotech Inc., https://www.raybiotech.com/covid-19-spike-ace2-binding-assay-kit-en/?variation_id=107121). Recombinant SARS-CoV-2 spike RBD protein coated wells were treated with the compounds (rucaparib, stenoparib, olaparib) in the range of concentration from 1 μM up to 500 μM and then incubated for 16 h at 4°C. Next, the recombinant hACE2 protein was added and the protocol provided by the manufacturer was followed. In brief, unbound hACE2 protein was removed by washing, and binding was assessed based on HRP-conjugated IgG in the presence of 3,3′,5,5′-tetramethylbenzidine (TMB) substrate. The HRP-conjugated IgG binds to the hACE2 protein and reacts with the TMB solution, producing a blue colour that is proportional to the amount of bound hACE2. The HRP-TMB reaction is halted with the addition of the Stop Solution, resulting in a blue-to-yellow colour change. The intensity of the yellow colour is then measured by absorbance at 450 nm with a microplate reader SpectraMax® iD5 (Molecular Devices, LLC., San Jose, CA, USA). Data points were obtained as average of duplicates and IC_{50} curves were fitted by nonlinear regression using GraphPad Prism.

2.20 | Molecular modelling

We have used the FTMap protein mapping algorithm to identify possible binding sites on the protein–protein interaction surface of the spike protein receptor-binding domain (RBD) versus the human ACE2 receptor (Brenke et al., 2009; Kozakov et al., 2015). Briefly, the FTMap method distributes small organic probe molecules on a dense grid defined on the protein surface, finds the most favourable positions for each probe type and identifies preferred binding hotspots as regions that bind multiple probe clusters. Here, we have used the experimentally determined structures of the ACE2-RBD complex for the B.1.5 ("Wuhan," PDB ID: 6M0J) (Lan et al., 2020), B.1.617.2 ("Delta," PDB ID: 7WBQ) and B.1.1.529 ("Omicron," PDB ID: 7WBP) variants (Han et al., 2022) and observed exactly one binding hotspot at the protein–protein interaction surface of all three variants, characterized by the residues 493–498, with further sidechains R403, E406, Y449, Y453, N501 and Y505 in the vicinity. After preparing the structure of rucaparib with LigPrep (Sastry et al., 2013), ligand docking was carried out with the single precision (SP) mode of Glide (Friesner et al., 2004; Halgren et al., 2004), and the binding mode was visualized with Maestro.

2.21 | Sequence homology alignment

Spike protein amino acid sequence was retrieved from https://viralzone.expasy.org/9556. Sequences were retrieved for the wild-type (https://www.uniprot.org/uniprot/P0DTC2), the alpha (https://www.ncbi.nlm.nih.gov/protein/QWE88920), the beta (https://www.ncbi.nlm.nih.gov/protein/QRN78347), the gamma (https://www.ncbi.nlm.nih.gov/protein/QVE55289), the delta (https://www.ncbi.nlm.nih.gov/protein/QWK65230), the omicron BA.1 (https://www.ncbi.nlm.nih.gov/protein/UFO69279.1?report=fasta), the omicron BA.2 (https://www.ncbi.nlm.nih.gov/protein/UJE45220.1?report=fasta), the omicron BA.2.12 (https://www.ncbi.nlm.nih.gov/protein/UMZ92892.1?report=fasta), the omicron BA.4 (https://www.ncbi.nlm.nih.gov/protein/UPP14409.1?report=fasta), the omicron BA.5 (https://www.ncbi.nlm.nih.gov/protein/UOZ45804.1?report=fasta) and the epsilon (https://www.ncbi.nlm.nih.gov/protein/QQM19141) variants. The relevant parts of the sequence were aligned using the ClustalW algorithm (https://www.genome.jp/tools-bin/clustalw). All sites were accessed on the 1st April 2022 with the exception of omicron BA.2.12, omicron BA.4 and omicron BA.5 sequences that were accessed on the 14th July 2022.

In the figure, conserved amino acids as compared with the wild-type variant are in green. The non-conserved amino acids are represented in red.

2.22 | Expression and purification of the SARS-CoV-2 spike protein and its receptor binding domain

The receptor-binding domain (RBD) of the SARS-CoV-2 virus spike protein (^{319}Arg-^{541}Phe) (Wuhan-Hu-1, Omicron BA.1, Omicron BA.5) was used in the experiments. Suspension HEK-293 cells stably expressing the RBD secreted to the culture media were created by the Sleeping Beauty transposon method using the p10-IRES2-eGFP vector construct as in a different application, described previously (Mayer & Meyer, 2001).

The Wuhan RDB sequence, as produced by Amanat et al. (2020), was inserted to the Sleeping Beauty transposon plasmid. The sequence on the N-terminal includes a signal peptide responsible for the secretion of the protein to the culture media and 6× His tag was introduced on the C-terminal. The plasmid was modified to produce the Omicron BA.1 and BA.5 RBD by replacing the Wuhan RBD coding sequence in the p10 plasmid for the Omicron BA.1 and BA.5 RBD coding sequences (modified sequences were synthetized via GeneArt Gene Synthesis, Invitrogen, Thermo Fisher Scientific). The Wuhan-Hu-1, Omicron BA.1 and Omicron BA.5 RBD-producing HEK293 cell lines were generated and cultured with the same procedure. Shaken cultures of suspension-adapted HEK293 cells were grown in a serum-free FreeStyle 293 expression medium (Gibco, Waltham, MA, USA, Cat. no. 12338018) incubated at 37°C and 5% CO_2, shaken at 100 rpm. The cells were sub-cultured every 3–4 days with seeding densities of 2×10^5 cells·ml^{-1} to promote cell growth and scale-up. The RBD was produced in a 300-ml shake flask cell culture. Cells were removed after 5–6 days by centrifugation (20 min, 250 x *g*; Rotanta 460R, Hettich, Kirchlengern, Germany). The purification of RBD was accomplished by immobilized nickel ion affinity chromatography. The supernatant was loaded into a 5-ml HisTrap HP column (GE Healthcare, Chicago, IL, USA), which was connected to an FPLC system (ÄKTA pureTM, GE Healthcare, Chicago, IL, USA). Protein bound to the column was eluted by imidazole (200 mM, pH 7.4). The protein-containing fraction was concentrated while the elution buffer was replaced by 0.2-M phosphate buffer (pH 6.8) using a centrifugal filter device. Centrifugation (Rotanta 460R, Hettich, Kirchlengern, Germany) was performed at 4000 x *g* for 20 min using a 10-kDa MWCO filter (Amicon Ultra 4, Merck KGaA, Darmstadt, Germany). The purity of the produced protein was confirmed by SDS-PAGE and the protein concentration was determined by UV-Vis spectroscopy at 280 nm.

2.23 | Nuclear magnetic resonance (NMR)-based investigation of spike-rucaparib interaction

Solution phase NMR experiments were performed under the following conditions.

The RBD of spike (~28 kDa) + rucaparib camsylate assay mixture contained 33-μM RBD (in 540 μl) and 1-mM rucaparib (dissolved in DMSO-d_6 in 20 μl) + 10% D_2O for lock in sodium-phosphate buffer (0.2 M, pH 6.8). Rucaparib was in ~30-fold excess. The RBD and rucaparib were assessed also without the other partner under the same conditions as references.

Bruker Avance Neo 700-MHz spectrometer (Bruker, Billerica, MA, USA) equipped with a Prodigy TCI cryoprobe was used. Experiments were run at 298-K temperature, and 10% D_2O was added to the solution for stabilizing the magnetic field via the ^{2}H lock channel. Typical 90° ^{1}H pulse duration was 11.5 μs. The residual DMSO-d_6 signal (2.59 ppm) was used as ^{1}H chemical shift reference. The NMR verification of the structure of rucaparib-camphor sulfonic acid (camsylate) salt was carried out in pure DMSO-d_6 solvent and yielded a full assignment of all ^{1}H and ^{13}C signals (spectra not shown). The assignments of aromatic (H15, H16, H18, H19) and olefinic (H11, H13) protons could be easily transferred to the buffer, containing rucaparib with or without the RBD protein. Excitation sculpting water suppression ^{1}H-NMR spectra using manufacturers 'zgesfpgp' pulse sequence was applied (Figure S1A) (Hwang & Shaka, 1995). The drug ligand signal appears as sharp signals while the protein signals are weak and broad (due to concentration and MW differences). A relatively strong and well-separated RBD signal at 0.4 ppm was selected for selective irradiation in STD-NMR (saturation transfer difference) experiments (weaker RBD signals below 0 ppm were also tested, and gave observable, but weaker responses) (Kövér et al., 2007; Mayer & Meyer, 2001; Unione et al., 2022; Viegas et al., 2011). For STD, we used manufacturers "stddiffgp19.3" pulse sequence with watergate water suppression (Piotto et al., 1992). Selective saturation was achieved using a series of 50-ms selective 90° Gaussian pulses, resulting in 2000-ms total irradiation time. The reference experiment was carried out identically, except that an off-resonance irradiation at −40 ppm was applied. A total of 12,160 scans interrupted with 2-s relaxation delays were co-added in both the on-resonance and the off-resonance (reference) experiments yielding 1 day total experiment time. In the difference spectrum of the two experiments (Figure S1A,B), the irradiated broad RBD signal is the strongest among protein signals, while the six protons of rucaparib ligand—probably closest to the binding site—gave the strongest responses. In the control experiment with no RBD protein, the rucaparib did not show the characteristic difference signals. An independent corroboration of rucaparib binding to RBD was carried out with the (non-selective) transferred NOESY (Meyer et al., 1997) experiment ("noesygpph19" pulse sequence). Again, the fingerprint signals gave cross-peaks with the same sign relative to the diagonal in the 2D NOESY map while they were missing in a sample without the protein.

2.24 | Isothermal titration calorimetry (ITC) measurements

ITC measurements were carried out on a MicroCal PEAQ-ITC microcalorimeter (Malvern Instruments, Worcestershire, UK) against three variants of the SARS-CoV-2 Spike protein receptor-binding domain

(RBD): wild-type (Wuhan strain), BA.1 and BA.5 variants. The buffer contained 20-mM phosphate, and the pH was set to 7.00. The protein was dissolved in the buffer and stored in 500-µl aliquots at −20°C. The concentration of the protein solution was 192 µM for the wild-type, 55.0 µM for the BA.1 variant and 20.0 µM for the BA.5 variant (the concentration values were verified on a NanoDrop 1000 spectrophotometer). The corresponding rucaparib solutions were prepared by dissolving the ligand in the same buffer at concentrations of 2.85 mM, 821 µM and 3.50 mM, respectively. The protein solution was thawed immediately before the ITC measurements, loaded into the sample cell and titrated at 25°C with the rucaparib solution. Injection volumes were 2 µl for the wild-type and BA.1 variants, and 1.5 µl for the BA.5 variant during the measurement. A total of 18 points were acquired per curve for the wild-type and BA.1 variants (excluding the first injection of 0.4 µl) and a total of 24 points for the BA.5 variant (excluding the first injection of 0.4 µl). The time between injections was 180 s for the wild-type and BA.1 variants, and 150 s for the BA.5 variant. The stirring rate was set to 750 rpm for all measurements.

Blank measurements were also performed at identical setups by loading buffer solution into the sample cell instead of protein solution. The acquired curves were corrected with the blank measurements, and outlier points were excluded from the fitting.

2.25 | Western blotting for spike detection

Primary HPAEpiC were seeded on six-well plates (2×10^5 cells per well) and transfected with 2-µg Covid-19 mRNA vaccine for 3 h. Cells were lysed in 100-µl RIPA buffer (50-mM Tris-HCl pH 8.0, 150-mM NaCl, 1% Triton X-100, 0.5% sodium deoxycholate, 0.1% SDS, 1-mM EDTA supplemented with 1-mM Na_3VO_4, 1-mM NaF, 1-mM PMSF and protease inhibitor cocktail). BCA protein assay (cat. no. 23227, Thermo Fischer Scientific, Waltham, MA, USA) was used for measuring protein concentration. Cell lysates were boiled with 6× SDS sample buffer (300-mM Tris-HCl, pH 6.8, 20% glycerol, 12% SDS, 0.05% bromophenol blue) supplemented with 5% β-mercaptoethanol. Protein extracts (10 µg) were separated by SDS-PAGE and then transferred onto nitrocellulose membranes using Bio-Rad Mini-Protean system; 5 µg recombinant purified SARS-CoV-2 Spike S1 protein was used as a positive control. Membranes were blocked with 5% (w/v) BSA/TBS containing 0.5% Tween 20 for 1 h, then incubated with anti-spike antibody overnight at 4°C. Peroxidase-conjugated antihuman IgG secondary antibody was applied for 1 h at room temperature. Immunoreactive bands were detected by enhanced chemiluminescence reaction and captured by ChemiDoc Touch Imaging System (Bio-Rad, Hercules, CA, USA).

2.26 | Western blotting for detection of NFκB activation

HPAEpiC cells (2×10^5) were seeded on six-well plates and treated with 0.5-µM rucaparib for 30 min and induced with 20-nM spike for up to 5 h or 2-µg vaccine for up to 3 h. Cells were lysed in 100-µl RIPA buffer (50-mM Tris-HCl pH 8.0, 150-mM NaCl, 1% Triton X-100, 0.5% sodium deoxycholate, 0.1% SDS, 1-mM EDTA supplemented with 1-mM Na_3VO_4, 1-mM NaF, 1-mM PMSF and protease inhibitor cocktail) and then boiled with 6× SDS sample buffer (300-mM Tris-HCl, pH 6.8, 20% glycerol, 12% SDS, 0.05% bromophenol blue) supplemented with 5% β-mercaptoethanol; 20-µg total cell lysates were separated by SDS-PAGE and transferred onto nitrocellulose membranes. Membranes were blocked with 5% (w/v) BSA/TBS for 1 h and then were probed with anti-RelA/NFκB pSer276 antibody (Novus Biologicals, cat.no. NB100-82086) overnight at 4°C. Anti-rabbit-HRP secondary antibody was applied then for 1 h at room temperature. Chemiluminescent signals were detected by ChemiDoc Touch Imaging System (BioRad, Hercules, USA).

2.27 | RT-qPCR

Total RNA from cells was isolated using TRIzol reagent (cat. no. 15596018, Invitrogen, Carlsbad, CA, USA); 2-U DNaseI (cat.no A2222, Thermo Fischer Scientific, Waltham, MA, USA) per 10 µg total RNA was used for DNase treatment, and 1-µg total RNA was reverse transcribed using High-Capacity cDNA Reverse Transcription Kit (cat. no. 4368814, Applied Biosystems, Foster City, CA, USA) according to the manufacturer's instructions. The reverse transcription reaction mixtures were supplemented with RNase inhibitor (cat.no 8080119, Applied Biosystems, Foster City, CA, USA). The qPCR reaction mixtures were prepared using qPCRBIO SyGreen Lo-ROX Supermix (PCR Biosystems Ltd., London, UK) and 20 ng (40 ng for IL-7) diluted cDNA with the appropriate primers at 500-nM final concentration. Amplification reactions were performed in 10-µl total volume using LightCycler 480 system (Roche Applied Science, Basel, Switzerland). Cycling conditions are given in Table S4. Expressions of target genes were normalized to GAPDH. The characteristics of the RT-qPCR reactions are reported according to the MIQE guidelines (Bustin et al., 2009) in Table S5.

2.28 | Transcription factor activation assay

Human PBMC were differentiated to macrophages as described above. Cells were induced with the spike protein of SARS-CoV-2 (20 nM, 24 h) and were treated with rucaparib in the concentrations indicated. Cells were then scraped and whole cell lysates were used to perform transcription factor binding assays using the Stat family TransAm kit (ActiveMotif, Tegernheim, Bayern, Germany, Cat. No. 42296).

2.29 | Data and statistical analyses

All experiments were repeated on at least three separate occasions, often with multiple parallel replicates processed on the same day but

treated as independently as possible. In plate-based assays, plate layout was varied among repeated experiments. All graphs and statistical analyses were generated using GraphPad Prism v.8.0.1 software. Statistical tests are indicated in the Figure legends, and the statistical tests can be accessed in the primary data files. *P* values less than 0.05 were considered statistically significant. Statistical analysis complied with the Data and Statistical Analysis guidance from the *BJP* (Curtis et al., 2022).

2.30 | Materials

Rucaparib was a generous gift from Dr. Thomas Harding, Clovis Oncology (Boulder, CO, USA). Comirnaty Original/Omicron BA.1, 15/15 mcg (tozinameran/riltozinameran) mRNA vaccine (GD6798) was supplied by Pfizer (New York, NY, USA) and recombinant spike protein (AGX818) by Merck (Rahway, NJ, USA). LPS (L4516) and olaparib (SML1858) were supplied by Sigma (St. Louis, MO, USA) and IKK16 (S2882), stenoparib (E7449) and talazoparib (BMN 673) were supplied by Selleck Chemicals (Houston, TX, USA). All routine chemicals were obtained from Sigma (St. Louis, MO, USA) unless stated otherwise. The suppliers of antibodies (with RRID), assay kits, cell lines, viruses, siRNA, and oligonucleotides are listed in the Supplementary information, as Table S1.

2.31 | Nomenclature of targets and ligands

Key protein targets and ligands in this article are hyperlinked to corresponding entries in the IUPHAR/BPS Guide to PHARMACOLOGY (http://www.guidetopharmacology.org) and are permanently archived in the Concise Guide to PHARMACOLOGY 2023/24 (Alexander, Fabbro et al., 2023; Alexander, Kelly et al., 2023)

3 | RESULTS

3.1 | Extensive oxidative stress and PARP activation in the lungs of COVID-19 patients

First, we assessed lung tissue samples from 15 patients with COVID-19 and a control group of 10 patients who died of non-pulmonary causes. We observed oxidative stress, marked by 4HNE staining, and PARP activation, marked by PAR immunostaining, in the pneumocytes, endothelial cells and macrophages of the lung tissue of COVID-19 patients, compared with controls (Figure 1a). There was a correlation between spike protein intensity and the per cent of 4HNE-positive cells, along with a correlation between PAR staining intensity and the per cent of PAR positive cells (Figure 1b). Furthermore, the per cent of 4HNE-positive cells correlated with both the PAR staining intensity and the per cent of PAR positive cells (Figure 1b). These data provide evidence for oxidative stress-induced PARylation events in a SARS-CoV-2-dependent fashion in COVID-19 and suggest the applicability of PARP inhibitors in COVID-19.

3.2 | Rucaparib can inhibit virus binding to target cells through disrupting the ACE2-spike protein interaction in suprapharmacological concentrations

Next, we assessed three approved PARP inhibitors, rucaparib, talazoparib and olaparib in a cellular SARS-CoV-2 infection model in concentrations ranging up to 40 μM. Rucaparib inhibited the infection and proliferation of the B.1.5 variant of SARS-CoV-2 virus—original Wuhan variant with D614G mutation (Korber et al., 2020) with IC_{50} = 27.5 μM, while talazoparib and olaparib had no effect (Figure 2). Importantly, rucaparib was not toxic at concentrations that profoundly inhibited viral proliferation, although these data suggest a narrow therapeutic window (the IC_{50} value for cell viability was 64.8 μM; Figure 2). Hence, the application of the inhibitor may result in toxicity.

The IC_{50} of rucaparib for viral replication (27.5 μM corresponding to ~8.7 $mg{\cdot}L^{-1}$) is much higher than that achieved at the recommended dose (600 mg BID, steady state level ~2.4 $mg{\cdot}L^{-1}$; Shapiro et al., 2019); furthermore, PARP inhibition of >90% is achieved using doses of 92 mg (Drew et al., 2016). Therefore, the impact on viral replication may result from binding to other targets. We investigated two potential targets for rucaparib, hexose-6-phosphate dehydrogenase (H6PD) and the spike protein.

Knezevic et al. (2016) suggested that rucaparib can bind to H6PD at an IC_{50} value of 18 μM, that is in the same range as the IC_{50} value we determined in the present study. We assessed the uptake of pseudovirions bearing the spike protein of SARS-CoV-2 (wild-type variant) in cells, where H6PD was silenced. Here, we applied a combination of siRNAs that were able to effectively silence H6PD (Figure 3a). Interestingly, siRNA-mediated silencing of H6PD abolished the inhibitory effect of rucaparib (Figure 3b).

The other potential target was the spike protein of SARS-CoV-2. Rucaparib bound directly to the spike protein of SARS-CoV-2 (IC_{50} = 115 ± 21.9 μM) in an in vitro assay, while no significant binding was detected for the other PARP inhibitors stenoparib and olaparib at concentrations up to 500 μM (Figure 4a). We observed magnetisation transfer from the receptor-binding domain (RBD) of spike to rucaparib in saturation difference spectrum NMR (STD-NMR) experiments that verifies rucaparib binding to the RBD in vitro (Figure 4b).

To understand the molecular basis of the binding affinity of rucaparib, we identified the putative binding site of rucaparib at the ACE2 interacting surface of the Spike protein of the B.1.5 ("Wuhan"), B.1.617.2 ("Delta") and B.1.1.529 ("Omicron") strains of SARS-CoV-2, with the FTMap protein mapping algorithm (Brenke et al., 2009). Exactly one binding hotspot was identified at the protein–protein interaction surface of all three strains (Figure 4c), characterized by the

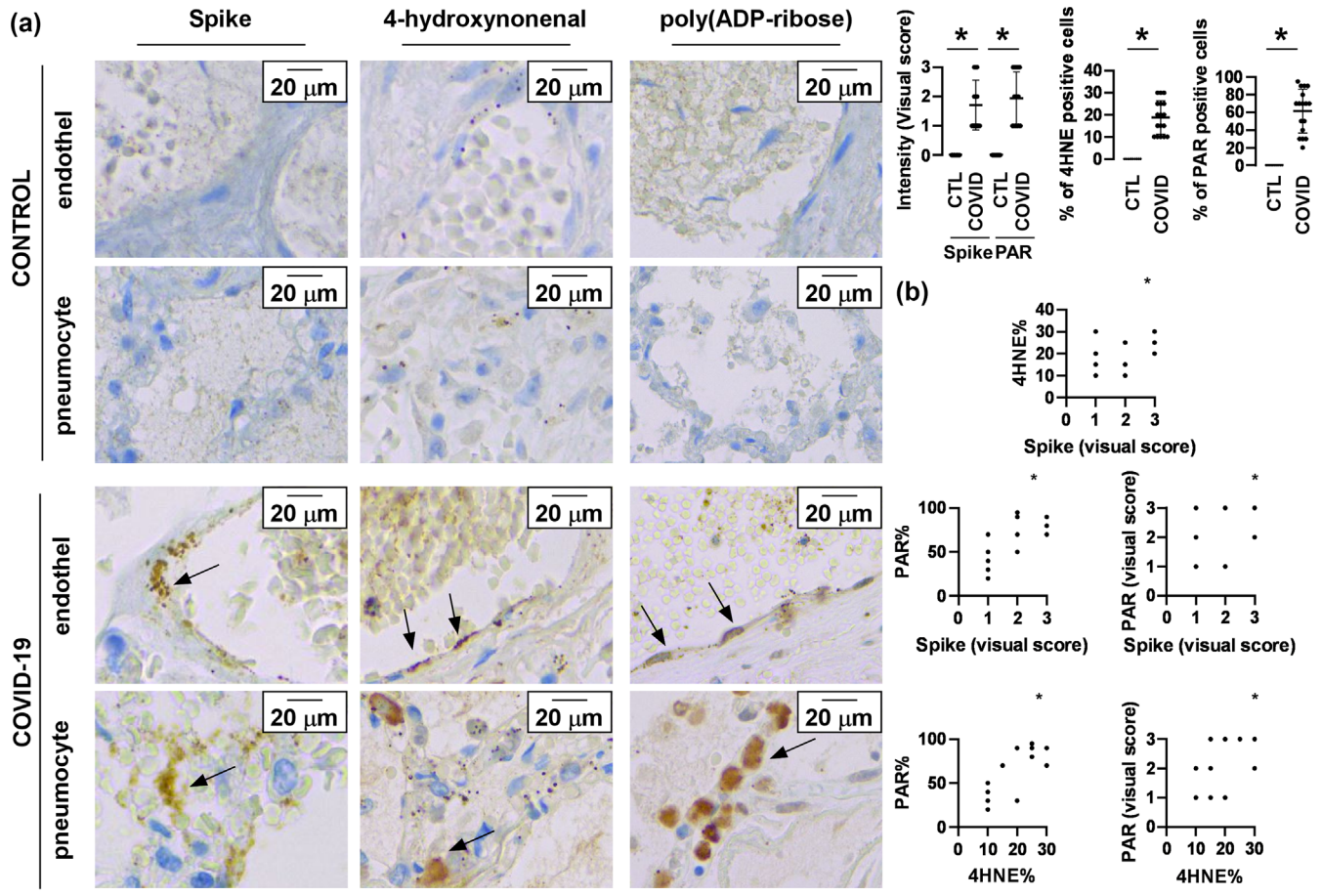

FIGURE 1 Oxidative stress and strong PARylation characterize COVID-19 disease. (a) In the lungs of 10 controls and 15 patients who died of COVID-19 SARS-CoV-2 spike protein, 4-hydroxynonenal and poly(ADP-ribose) immunohistochemistry was performed and evaluated. The intensity of staining for spike, 4-hydroxynonenal and PAR were scored 0–3, and the PAR positive nuclei were counted and expressed in per cent. Data shown are averages ± SD. * $P < 0.05$, significantly different as indicated; two-tailed t test. (b) The obtained histological scores were correlated with each other, using Spearman correlations.*$P < 0.05$, significant correlation between scores. The numerical values of the Spearman correlations and the corresponding P values are presented in Table S8. Abbreviations: CTL—control, 4HNE—4-hydroxynonenal, PAR—poly(ADP-ribose).

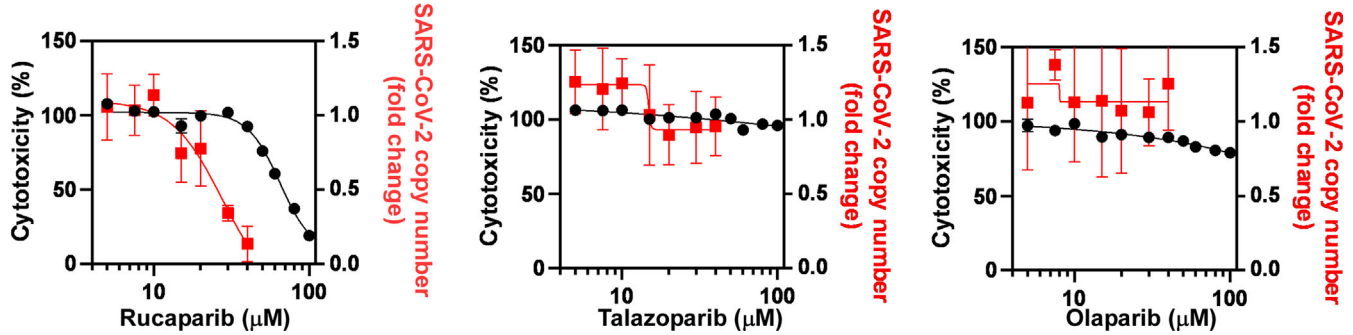

FIGURE 2 Rucaparib, but not olaparib and talazoparib, inhibits the binding of SARS-CoV-2 to the host cell. The antiproliferative and cytotoxic effects of rucaparib, olaparib and talazoparib were tested on Vero E6 cells infected with B.1.5 variant SARS-CoV-2 (n = 3). Data shown are averages ± SD. IC_{50} values were obtained by non-linear regression ([inhibitor] vs. response—variable slope (four parameters) mode of GraphPad).

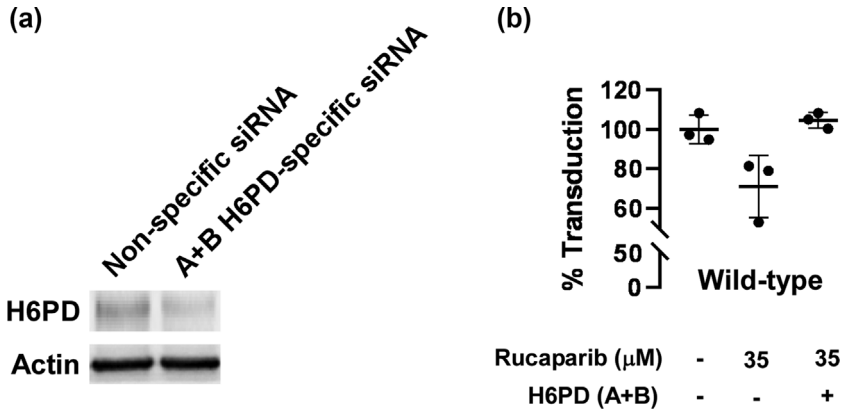

FIGURE 3 Rucaparib does not exert its antiviral effects through inhibiting hexose-6-phosphate dehydrogenase. (a) The efficiency of silencing was determined by western blot in engineered HEK293T cells in which H6PD was silenced using siRNA as described in Section 2 (n = 1). (b) Fluorescently-labelled pseudovirion uptake was assessed in HEK293T cells (n = 3). Data shown are averages ± SD.

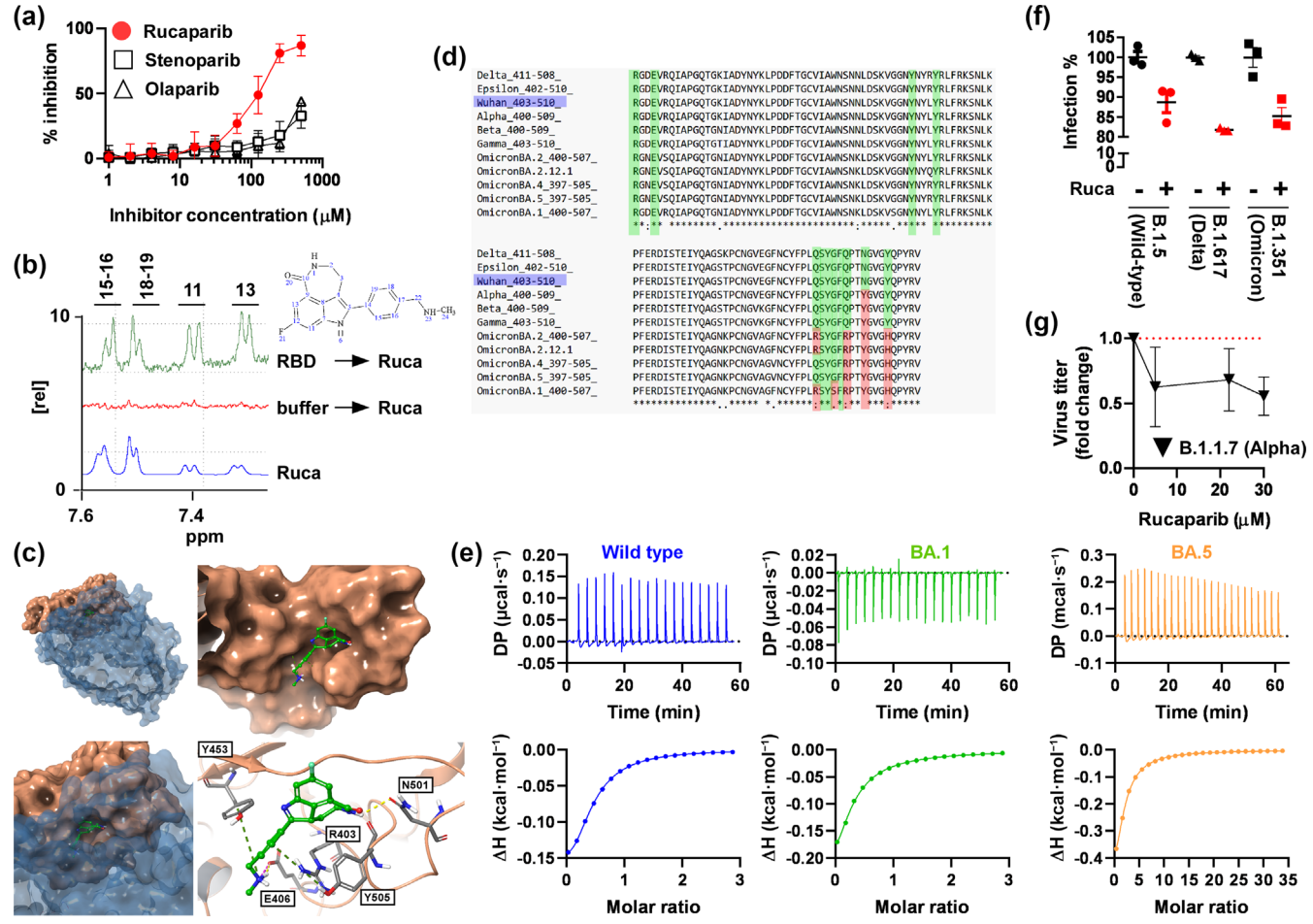

FIGURE 4 Rucaparib binds to the spike protein of SARS-CoV-2 and inhibits virus uptake. (a) The indicated PARP inhibitors were tested to block the spike-ACE2 interaction in an in vitro binding assay (n = 2). (b) STD-NMR spectrum of rucaparib alone and in complex with the receptor-binding domain of spike. (c) Predicted binding mode of rucaparib (green) at the protein–protein binding surface of the SARS-CoV2 RBD (fawn), with the main protein–ligand interactions highlighted as dashed lines (magenta: ionic interaction, yellow: H-bond, green: cation-pi interaction). (d) The sequence of the rucaparib binding site from the available variants were compared. The wild-type Wuhan strain is marked in blue. (e) ITC curve acquired by the titration of the spike protein RBD solution of the indicated strains with rucaparib solution. The top panel is the thermogram while the bottom one is the fitted curve after blank correction and peak integration. The sixth point (after the first 0.4-μl injection) was excluded from the fitting. (f) Fluorescently-labelled pseudovirions were pre-treated with 35-μM rucaparib and pseudovirus uptake was assessed in HEK293T cells (n = 3). (g) The alpha variant of SARS-CoV-2 was pretreated with rucaparib and was used to infect Vero E6 cells (n = 3). Data shown are averages ± SD. Abbreviations: DP—change in power, RBD—receptor binding domain, Ruca—rucaparib.

residues 493–498, with further sidechains R403, E406, Y449, Y453, N501 and Y505 in the vicinity (Figure 4c) (Friesner et al., 2004; Halgren et al., 2004). Next, we predicted the binding mode of rucaparib with ligand docking by the Glide module of the Schrödinger drug design suite (Figure 4c). The proposed binding mode presents a reasonable shape complementarity between the binding site and the ligand and is stabilized mainly by a strong ionic interaction between the negatively charged E406 sidechain and the terminal methylamine group of rucaparib. The latter is a positively charged and highly flexible moiety that is exclusive to this compound among the four PARP inhibitors tested in this study, which is in line with the exclusive on-target affinity of rucaparib. Additional interactions involve an H-bond between N501 and the NH group of the lactam unit, and back-to-back cation-pi interactions between Y453 and the methylamine group, as well as R403 and the phenyl ring. The STD-NMR shows magnetisation transfer (Figure 4c) from RBD to H15, H16, H18 and H19 of the aromatic moiety of rucaparib that verifies binding and the validity of the in silico docking (Figure 4c). Most of the amino acids responsible for rucaparib binding were conserved among SARS-CoV-2 de-escalated (wild-type, alpha, beta, gamma, delta, epsilon, omicron BA.1, omicron BA.2, omicron BA.2.12) and currently spreading variants (omicron BA.4, omicron BA.5). The omicron variants, and among them, the omicron BA.1 variant harboured the highest number of mutations at the binding site (Figure 4d). Amino acid changes can be considered homologous based on the homology scores obtained from the BLOSUM62 (Pearson, 2013), the Protsub (Jia & Jernigan, 2021) and the VTML200 (VTML200 amino acid homology matrix, 2023) matrices with the exception of N501Y that has a low homology score (Table S6). The mostly homologous changes to the amino acids of the binding site explains why rucaparib can still bind to newly emerging variants, such as the B1.351 omicron variant and makes it very likely that rucaparib can neutralize the currently spreading variants. This hypothesis is verified by ITC measurements, direct binding with dissociation constant values (K_d) of 47, 38.3 and 73.5 μM could be observed between rucaparib and the wild-type, BA.1 and BA.5 spike protein constructs, respectively, verifying that amino acid changes do not reduce the binding of rucaparib (Figure 4e, Table S7).

We also tested the binding of rucaparib to spike protein in cell-based assays by preincubating rucaparib with a pseudovirus bearing the spike protein of SARS-CoV-2 (wild-type, delta and the omicron variants) or the SARS-CoV-2 virus (alpha variant). Rucaparib inhibited virus uptake of all major variants of SARS-CoV-2 (Figure 4f,g), suggesting that it inhibits the binding of many strains to host cell receptors.

3.3 | Rucaparib does not interfere with the macrodomain of SARS-CoV-2

SARS-CoV-2 has a macrodomain to remove single ADP-ribose units added to viral proteins by the cellular mono-ADP-ribosylation machinery as a protective measure against virus infection (Alhammad et al., 2021; Caprara et al., 2018; Daugherty et al., 2014; Fehr et al., 2020; Guo et al., 2019; Russo et al., 2021; Tauber et al., 2021; Xing et al., 2021). In order to exclude the possibility that rucaparib was acting via an interaction with the macrodomain of SARS-COV-2, we assessed whether rucaparib, in concentrations corresponding to those established above, targets the macrodomain of SARS-CoV-2 by applying a previously described model (Russo et al., 2021). In agreement with previous results (Russo et al., 2021), Interferon-γ (IFNγ) treatment induced substantial cellular ADP-ribosylation (note that the detection reagent recognizes mono-, oligo- and poly(ADP-ribose)), which was reduced by ~50% when the macrodomain of SARS-CoV-2 was overexpressed (Figure 5a). Rucaparib treatment at either 500 nM or 20 μM did not prevent this macrodomain-dependent reduction in IFN-induced ADP-ribosylation relative to control cells (Figure 5a), suggesting that rucaparib does not inhibit the viral macrodomain at the concentrations tested. However, we observed a concentration-dependent effect of rucaparib on the overall induction of ADP-ribosylation by IFN-γ, indicating an inhibitory effect on IFN-induced ADP-ribosylation (Figure 5a). This was not due to reduced IFN signalling, as rucaparib did not interfere with IFNγ or poly(I:C)-induced Stat-1 phosphorylation (Figure 5b–e). We also assessed the activation of members of the Stat family (Stat1, 3, 5A, 5B) upon spike protein induction in human macrophages. Stat1 and Stat3 were activated upon spike induction that was not inhibited by rucaparib (Figure 5e). Interestingly, Stat5A and 5B activation was inhibited by spike protein, but no statistically significant changes to Stat5A and 5B were elicited by rucaparib treatment (Figure 5e). We conclude that rucaparib does not affect IFN signalling or the viral macrodomain but may inhibit IFN-induced PARP activity.

3.4 | Rucaparib has anti-inflammatory properties in pharmacological concentrations in the cell models of COVID-19

As PARP activation is proinflammatory (Bai & Virag, 2012; Curtin & Szabo, 2020; Morrow et al., 2009), we correlated readouts of the complete blood count with the lung histology markers (spike protein intensity, per cent of 4HNE-positive cells, PAR intensity and per cent of PAR-positive cells) in the tissues from COVID-19 patients assessed previously. Lymphocyte number and lymphocyte per cent correlated with all histology markers (Figure 6, Table S8). Lymphocytopaenia is a common feature of a variety of viral infections and, in line with that, also characterizes COVID-19 (Wagner et al., 2020). These data suggest that immune response correlates with PARylation following ROS as well as with the viral load in COVID-19.

Given the proinflammatory properties of PARP activation that has been shown in multiple preclinical models, as well as in humans (Bai & Virag, 2012; Curtin & Szabo, 2020; Morrow et al., 2009), we assessed the capacity of rucaparib to inhibit the expression of cytokines associated with the cytokine release syndrome in COVID-19. First, we tested the anti-inflammatory properties of rucaparib on primary HPAEpiC, which were stimulated by recombinant spike protein or an RNA vaccine against a mixture of wild-type and omicron

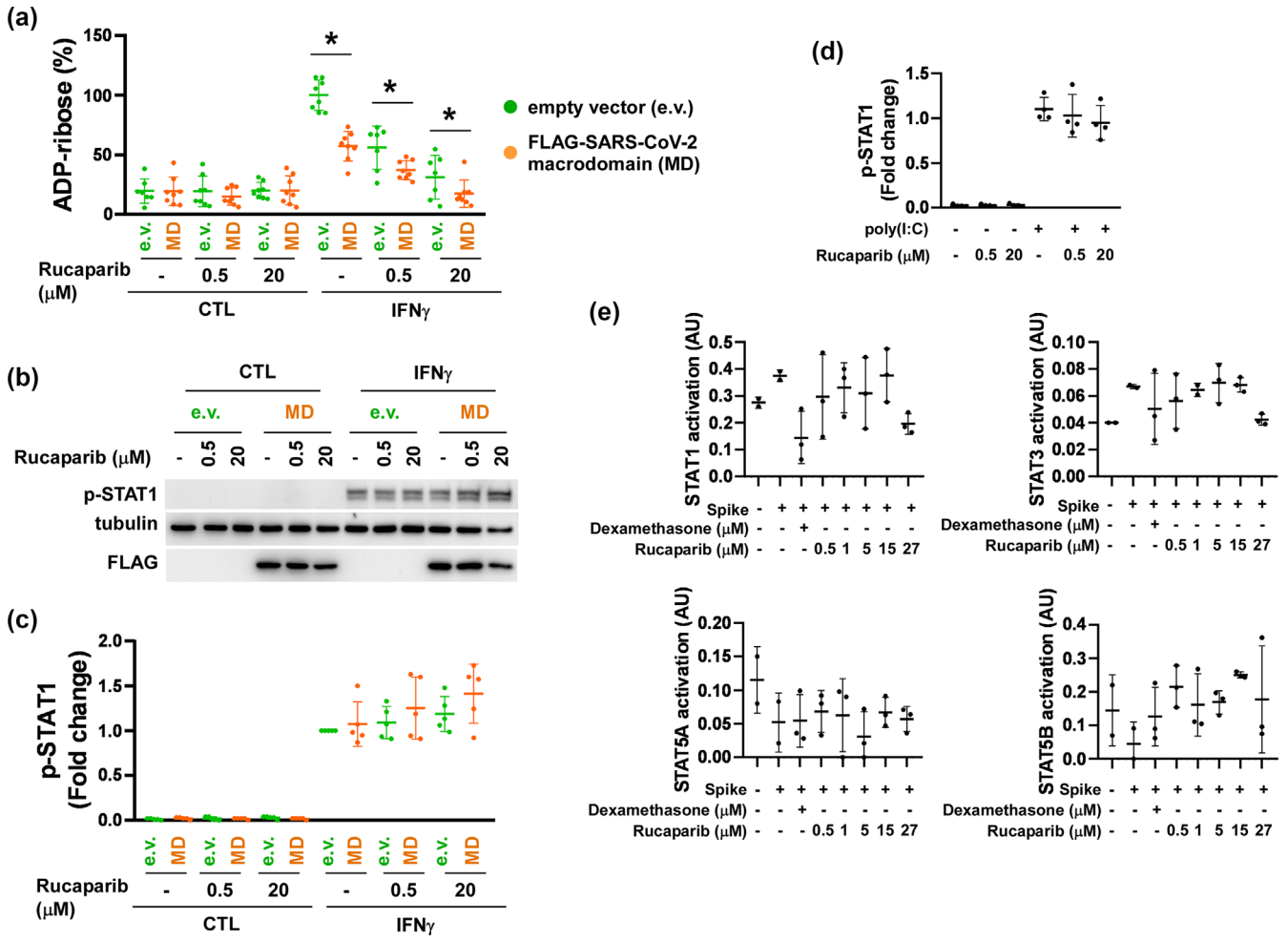

FIGURE 5 Rucaparib does not affect the function of the macrodomain of SARS-CoV-2 and does not interfere with the activity of the Stat transcription factor family. (a–c) A549 cells, either transduced with empty vector control (e.v.) or lentiviral constructs for FLAG-tagged SARS-CoV-2 macrodomain overexpression (MD) were treated with either vehicle or different combinations of 100 U IFNγ, 500 nM or 20-μM rucaparib for 24 h, as shown. ADP-ribosylation was detected by immunofluorescence (a, n = 8) and STAT1 phosphorylation (n = 5) and tubulin levels were determined by immunoblotting (b,c). All values were normalized to the IFNγ-treated e.v. control. Data shown are averages ± SD. Normality was checked. * $P < 0.05$, significant differences between the empty vector-transfected control cells and treated cells; one-way ANOVA. (d) A549 cells were induced with poly(I:C) and STAT1 phosphorylation was determined as described in Section 2 (n = 3). All values were normalized to the IFNγ-treated e.v. control. Numerical values are presented as the average ± SD. (e) Stat1, 3, 5A and 5B activation was determined in human macrophages using the TransAM kit as described in Section 2. One donor is displayed in the technical repeats indicated. Numerical values are presented as the average ± SD.

variants of SARS-CoV-2. Vaccine treatment modelled immune responses induced by viral RNA. Importantly, spike protein was not detectable in primary HPAEpiC at the end of the assay (Figure 7a); therefore, immune reaction was induced by viral RNA and not by spike protein. In other words, vaccine treatment models only the virus RNA-induced immunological effects. Both spike protein and viral RNA induced several interleukins, IL-6, IL-7, IL-1β and TNFα but not IL-1α, in lung epithelial cells, and the induction of these cytokines was inhibited by 0.5-μM rucaparib (Figure 7b).

Immune cells were also PAR positive in the lung tissue of COVID-19 patients. In line with that, in human macrophages, differentiated in vitro and challenged with the SARS-CoV-2 spike protein, the expression of IL-6 was induced. Such expression was suppressed by rucaparib (Figure 7c), suggesting that PARP activation is also a key player in regulating the inflammatory reaction of the immune cells in the lungs.

PARP1 is required for the activation of the transcription factor NFκB complex (Bai & Virag, 2012; Oliver et al., 1999). Primary HPAEpiC were treated with recombinant spike protein (up to 5 h), or vaccine (up to 3 h). Spike protein after 5 h, while vaccine treatment in the time window of 0.5–1 h, induced the ^{276}S phosphorylation of NFκB, highlighting NFκB activation (Antal et al., 2023) (Figure 8a). NFκB activation induced by spike or vaccine treatment, measured by detecting the phosphorylation of the ^{276}S residue and by assessing the nuclear translocation of NFκB, was down-regulated by rucaparib in 0.5-μM concentration (Figure 8a-c). These changes were equally blocked by

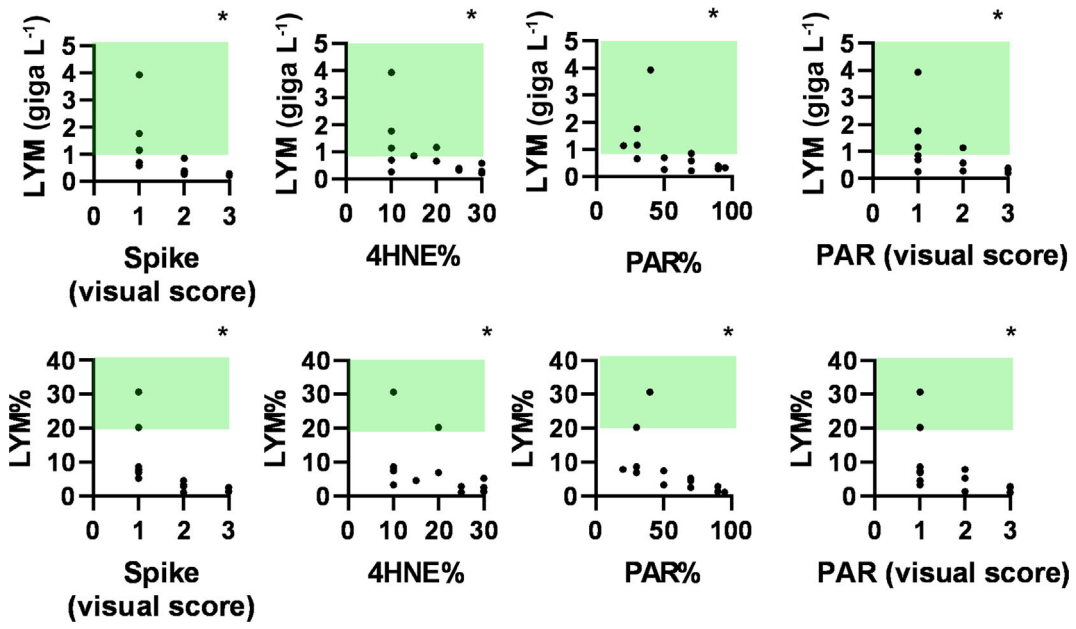

FIGURE 6 Oxidative stress and PARP activation correlates with leukocytopaenia. The indicated haemogram values were correlated with the indicated histology scores among the COVID-19 patient cohort (n = 13 cases). The Spearman correlation was calculated; * $P < 0.05$, significant correlation. The numerical values of the Spearman correlation and the individual *P* values are in Table S8. The green rectangles refer to the human reference range of the readouts. Abbreviations: CTL—control, LYM—lymphocyte, PAR—poly(ADP-ribose), 4HNE—4-hydroxynonenal.

IKK16, a specific inhibitor of NFκB kinase (Figure 8b,c) that is known to block NFκB activation (Waelchli et al., 2006). Importantly, both rucaparib and IKK16 reduced the mRNA expression of IL-1β (Figure 8d), a chemokine induced in COVID-19. Altogether, these data suggest that rucaparib can restrict NFκB activation and therefore elicit an anti-inflammatory phenotype.

4 | DISCUSSION

In the frame of this study, we assessed the applicability of pharmacological inhibition of PARP in COVID-19 disease and identified two activities of rucaparib, namely, neutralizing SARS-CoV-2 and anti-inflammatory properties.

A PARP inhibitor, stenoparib (E7449, previously also developed for cancer therapy) has already been shown to inhibit SARS-CoV-2 proliferation in low micromolar concentrations, although the mechanisms underpinning the effect were not investigated in depth (Zarn et al., 2022). Rucaparib inhibits SARS-CoV-2 proliferation with an IC_{50} value of 27.5 μM that is roughly three-fold higher than serum concentration achieved at the recommended dose (~8.7 $mg \cdot ml^{-1}$ vs. ~2.4 $mg \cdot L^{-1}$; Shapiro et al., 2019) suggesting off-target effects that are not related to PARP1 inhibition. We have identified two potential targets, the enzyme H6PD and the spike protein of SARS-CoV-2.

Rucaparib binds to H6PD with an IC_{50} value of 18 μM (Knezevic et al., 2016) suggesting H6PD as a possible target at the concentrations used in pseudovirus uptake experiments. H6PD plays a major role in maintaining the redox balance of cells through catalysing the first two reactions of the pentose-phosphate shunt in the endoplasmic reticulum (Senesi et al., 2010). Silencing of H6PD leads to oxidative stress (Cossu et al., 2020), which supports virus uptake (Foo et al., 2022) contrary to the observed disruption of rucaparib's inhibitory activity on virus entry. Furthermore, deficiency in the cytosolic isoform of H6PD (glucose-6-phosphate dehydrogenase) does not affect the outcome of severe COVID-19 and decreases the likelihood of developing severe COVID-19 (Kumar et al., 2021). Altogether, these findings suggest that H6PD is unlikely to be a major target of rucaparib.

In terms of another possible target, our data showed that rucaparib can bind to the spike protein of SARS-CoV-2 and therefore inhibit the binding of SARS-CoV-2 to the ACE2 receptor and subsequent virus entry into host cells. Interestingly, olaparib and talazoparib had no effect on SARS-CoV-2 infection and proliferation. Rucaparib not only neutralized all the variants assessed in this study but was also shown to bind to the omicron BA.1 variant, which has the most mutations among the amino acids responsible for rucaparib binding, with a K_d value similar to that for binding to the wild-type virus. These results indicate that rucaparib is likely to be active against the currently spreading and potentially future variants, strengthening the applicability to block SARS-CoV-2 binding. Furthermore, the rucaparib binding site is a potential site for further drug development to target the SARS-CoV-2–ACE2 interaction.

We detected oxidative stress and PARylation in the lungs of COVID-19 patients, similar to previous reports (Abouhashem et al., 2020; Fodor et al., 2021; Heer et al., 2020; Karu et al., 2022; Montiel et al., 2022; Tangos et al., 2022). A large set of studies have provided evidence that PARP activation is pro-inflammatory (Bai &

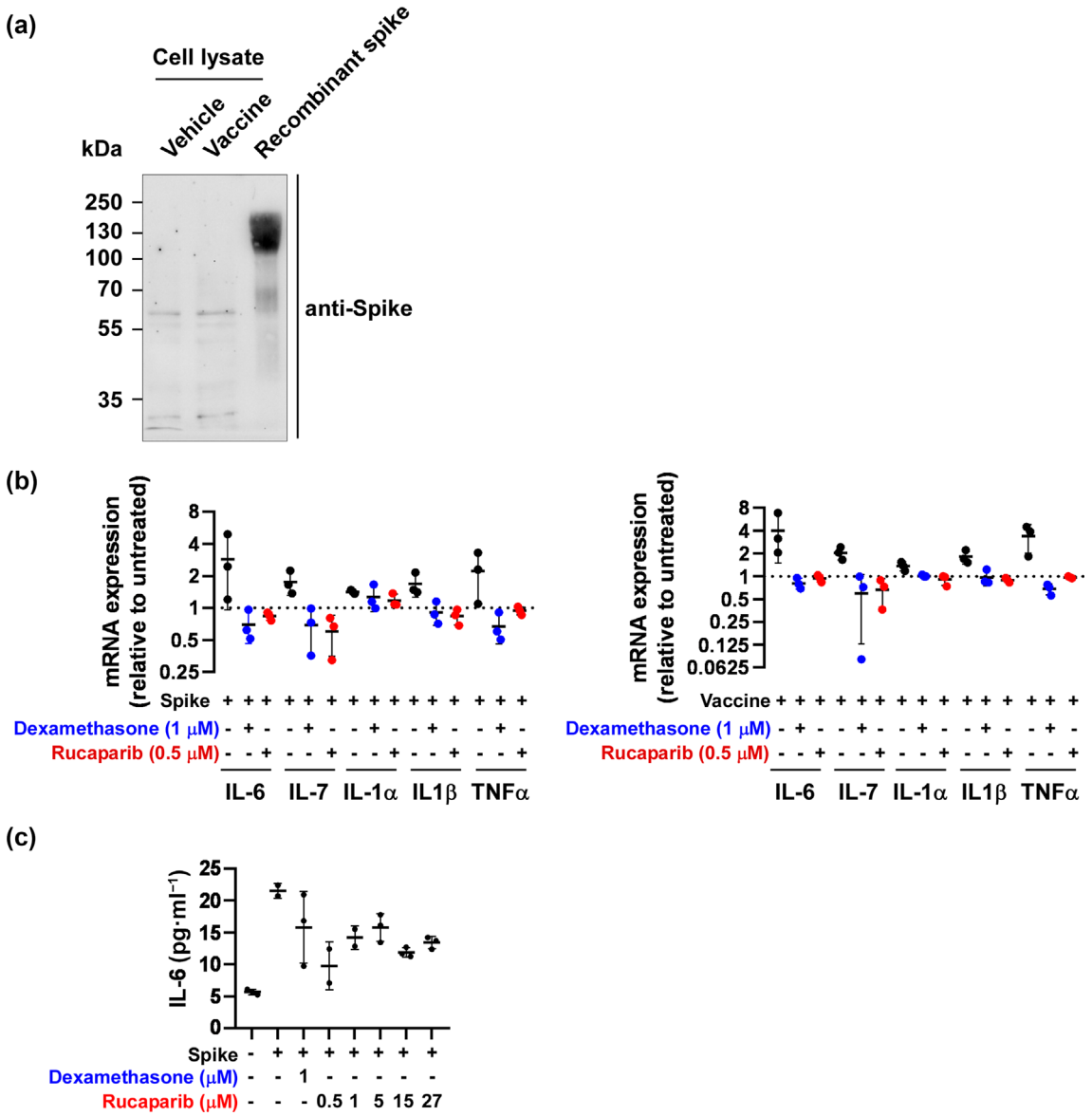

FIGURE 7 Rucaparib inhibits spike and virus RNA-induced proinflammatory cytokine production. (a) Primary human pulmonary alveolar epithelial cells ($2 * 10^5$) were treated with 2-μg vaccine for 3 h. Then cells were harvested and spike expression was assessed by SDS-PAGE and western blot (n = 1). Blots were retrieved using the antibodies indicated. (b) Primary human pulmonary alveolar epithelial cells (8×10^4 per well) were seeded to 12-well plates, pretreated with 0.5-μM rucaparib or 1-μM dexamethasone for 30 min, then stimulated with 20-nM SARS-CoV-2 spike S1 protein or 0.8-μg Covid-19 mRNA vaccine (Comirnaty Original/Omicron BA.1) for 3 h (n = 3). Cells were harvested, RNA was isolated and qRT-PCR was performed with the indicated primers. The dashed line represents the level of the expression of the mRNA in question in vehicle-treated, non-stimulated cells. (c) Human primary monocytes differentiated to macrophages were treated as described in Section 2 and IL-6 production was measured (n = 3).

Virag, 2012; Curtin & Szabo, 2020; Morrow et al., 2009), suggesting an involvement of PARylation in the inflammatory response in COVID-19. Rucaparib proved to be anti-inflammatory in primary HPAEpiC and in human monocyte-derived macrophages stimulated by the spike protein of SARS-CoV-2 and virus RNA, with an efficacy similar to that of dexamethasone. Rucaparib down-regulated the NFκB-dependent expression and production of a set of proinflammatory cytokines (IL-6, IL-7, IL-1β and TNFα) in both models. Therefore, rucaparib can restrict both major inflammatory pathways induced by SARS-CoV-2. Our data suggest that the anti-inflammatory action of rucaparib depends on inhibition of NFκB. Submicromolar rucaparib concentrations, used in these studies, are pharmacologically relevant and are comparable to the achievable serum levels of rucaparib in humans (Shapiro et al., 2019; Wilson et al., 2017). In addition, we also showed that the level of oxidative stress and PARylation strongly correlated with the lymphocytopaenia that is associated with poor outcome in COVID-19 (Wagner et al., 2020), suggesting a correlation between lung PARylation and disease outcome.

Several other aspects of PARP-mediated inflammatory response have direct relevance to COVID-19-related inflammatory lung injury.

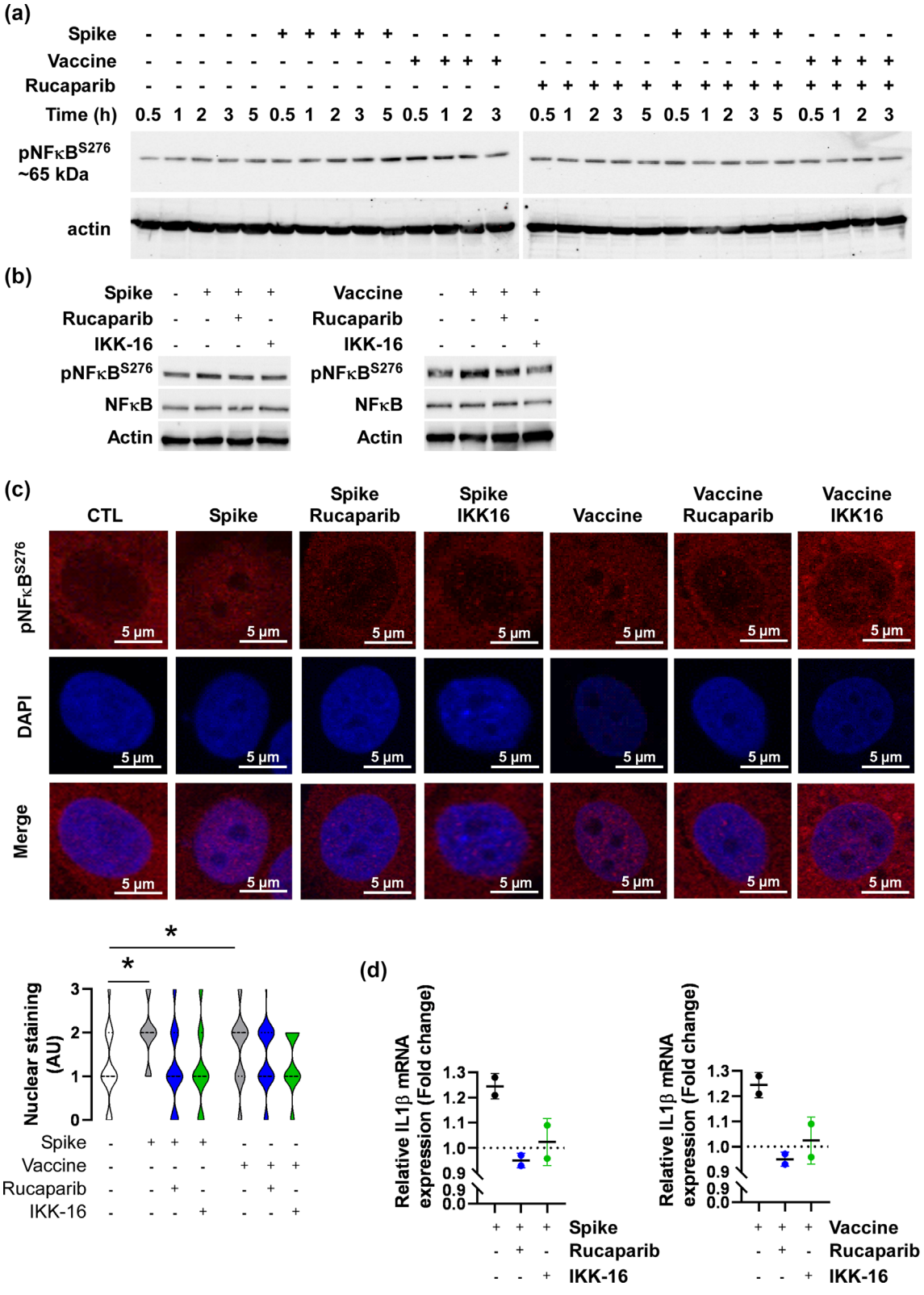

FIGURE 8 Legend on next page.

Genetic or pharmacological PARP inhibition was protective in asthma, acute lung injury (burn, smoke inhalation, bacterial infection, etc.), acute respiratory distress syndrome (ARDS), chronic obstructive pulmonary disease (COPD), lung fibrosis or ventilation-induced lung injury (see Curtin et al., 2020). Importantly, an overwhelming set of data point out that these findings can be translated to the human situation, for example, treatment with INO-1001, a PARP inhibitor, reduced serum IL-6 expression in humans (Morrow et al., 2009). The immunosuppressive effects of PARP inhibition in humans is further supported by a report (Liontos et al., 2021) showing that patients receiving PARP inhibitors, as oncological treatment, produced fewer neutralizing antibodies following SARS-CoV-2 vaccination, compared with healthy volunteers.

PARP9, PARP11 and PARP14 are implicated in antiviral protection, including SARS-CoV-2, being responsible for the PARylation of viral proteins (see Curtin et al., 2020) that is countered by the macrodomain of SARS-CoV-2 (Alhammad et al., 2021). Importantly, these enzymes are less susceptible for inhibition by clinically available PARP inhibitors (Wahlberg et al., 2012), suggesting that rucaparib does not strongly inhibit these PARP enzymes and does not block this intrinsic protective mechanism of cells. This is in agreement with our observation that rucaparib does not fully diminish PARylation induced by IFN-γ, despite fully inhibiting PARP1 and PARP2 at the concentrations we used, highlighting that PARP enzymes other than PARP1 and PARP2 are probably responsible for PARylation in response to viral infection (e.g. PARP9/DTXL3L complex; Russo et al., 2021). Furthermore, in line with these, rucaparib does not interfere with the IFN-γ pathway that is an organismal antiviral protective pathway. These observations strengthen the safety aspects of rucaparib treatment in SARS-CoV-2 infection.

Of note, there are other PARP-related events, relevant to COVID-19, which were not tested in our study. PARP overactivation can contribute to cell death and tissue damage (Curtin et al., 2020). Furthermore, PARP activation can strongly reduce cellular NAD+ levels (Curtin & Szabo, 2020) that has been implicated in the pathogenesis of COVID-19 (Heer et al., 2020).

Taken together, our results suggest that rucaparib has a dual action in COVID-19; it can inhibit virus entry through disrupting the binding of SARS-CoV-2 to ACE2 and also reduce the inflammatory response. To the best of our knowledge, this is the first drug with such a dual action. Although the IC_{50} value of rucaparib in disrupting the SARS-CoV-2 binding is higher than the steady state levels of the dose approved for cancer therapy, rucaparib could potentially be applied as an aerosol in patients to achieve higher local concentrations, so rucaparib can exert its dual effects in the lungs. Rucaparib, unlike the other clinically approved PARP inhibitors, was reported to continue to inhibit PARP1 for extended periods even after its removal (Murray et al., 2014; Smith et al., 2022), further strengthening the case for its repurposing. Rucaparib is also likely to block the currently spreading SARS-CoV-2 variants. Our results point towards a narrow therapeutic window at the high rucaparib concentrations required for blocking SARS-CoV-2 binding to target cells, based on the small differences between its pharmacologically active and toxic concentrations in cell models.

In terms of inhibiting the inflammatory response, rucaparib was active in low concentrations, suggesting that rucaparib can be repurposed to block inflammation in COVID-19 using the currently available dosing and formulation. Of note, the anti-inflammatory potential of rucaparib was comparable to that of dexamethasone, the standard of care in COVID-19, in the models used in this study. PARP inhibitors can potentially be synergistic with **tocilizumab** and anti-IL-6 monoclonal antibody used against the cytokine storm, as well as with the anti-inflammatory drugs used in the therapy of COVID-19. PARP inhibitors have a very favourable side effect profile (Curtin et al., 2020; Curtin & Szabo, 2020; LaFargue et al., 2019). These observations point towards the repurposing of rucaparib to treat acute COVID-19 and possibly long-COVID.

AUTHOR CONTRIBUTIONS

H. Papp performed and evaluated the experiments applying SARS-CoV-2 virus, wrote and revised the manuscript. E. Tóth performed immunology-related experiments upon spike and virus RNA induction, wrote and revised the manuscript. J. Bóvári-Biri and K. Bánfai prepared and differentiated human monocytes, wrote and revised the manuscript. P. Juhász performed the histological analysis of the COVID-19 patients, wrote and revised the manuscript. M. Mahdi performed and evaluated neutralization experiments using pseudoviruses, wrote and revised the manuscript. L.C. Russo performed and

FIGURE 8 Rucaparib exerts anti-inflammatory features through inhibiting NFκB activity. (a) Primary human pulmonary alveolar epithelial cells were plated into six-well plates (2×10^6 per well) and were pretreated with vehicle or 0.5-μM rucaparib for 30 min then treated with spike protein in 20-nM concentration or 2-μg vaccine for the indicated time. Cells were harvested, protein was extracted and analysed by SDS-PAGE followed by western blot that was probed with the indicated antibodies (n = 1). (b) Primary human pulmonary alveolar epithelial cells were plated into six-well plates (2×10^6 per well) and were pretreated with vehicle or 0.5-μM rucaparib for 30 min or 2-μM IKK16 for 24 h then induced with spike protein in 20-nM concentration for 3 h or 2-μg vaccine for 30 min (n = 1). Cells were harvested, and protein was extracted and analysed by SDS-PAGE followed by western blot that was probed with the indicated antibodies. (c) Primary human pulmonary alveolar epithelial cells (3×10^4) were grown on coverslips and immunofluorescent assay was performed and scored as described in Section 2 (n = 50 per group). * $P < 0.05$, significantly different from control; one-way ANOVA. (d) Primary human pulmonary alveolar epithelial cells (8×10^4 per well) were seeded in12-well plates, pretreated with 0.5-μM rucaparib for 30 min or 2-μM IKK16 for 24 h, then stimulated with 20-nM SARS-CoV-2 Spike S1 protein or 0.8-μg Covid-19 mRNA vaccine (Comirnaty Original/Omicron BA.1) for 3 h or 30 min, respectively (n = 2 per group). Cells were harvested, RNA was isolated and qRT-PCR was performed with the indicated primers. The dashed line represents the level of the expression of the mRNA in question in vehicle-treated, non-stimulated cells.

evaluated the experiments on SARS-CoV-2 macrodomain inhibition. D. Bajusz performed molecular modelling and wrote and revised the manuscript. A. Sipos performed cytokine and TransFactor measurements and wrote and revised the manuscript. L. Petri and T.V. Szalai performed and evaluated in vitro spike-ACE2 binding experiments and wrote and revised the manuscript. Á. Kemény performed cytokine measurements. M. Madai performed the experiments applying SARS-CoV-2 virus. A. Kuczmog performed the experiments applying SARS-CoV-2 virus. G. Batta performed and evaluated NMR experiments and wrote and revised the manuscript. O. Mózner cloned the RBD of SARS-CoV-2 spike protein and wrote and revised the manuscript. D. Vaskó and E. Hirsch expressed and purified the RBD of SARS-CoV-2 spike protein and wrote and revised the manuscript. P. Bohus provided patients lung samples and patient data. G. Méhes supervised histology and wrote and revised the manuscript. J. Tőzsér supervised the pseudovirus experiments and wrote and revised the manuscript. N.J. Curtin conceived the study and wrote and revised the manuscript. Z. Helyes wrote and revised the manuscript. A. Tóth made a major conceptual advance and wrote and revised the manuscript. N.C. Hoch supervised the macrodomain experiments and wrote and revised the manuscript. F. Jakab supervised the SARS-CoV-2 experiments and wrote and revised the manuscript. G.M. Keserű supervised in vitro binding studies and modelling and wrote and revised the manuscript. J.E. Pongrácz supervised the human monocyte experiments and wrote and revised the manuscript. P. Bai conceived and supervised the study and wrote and revised the manuscript.

AFFILIATIONS

[1]National Laboratory of Virology, University of Pécs, Pécs, Hungary
[2]Institute of Biology, Faculty of Sciences, University of Pécs, Pécs, Hungary
[3]Szentagothai Research Centre, University of Pécs, Pécs, Hungary
[4]Department of Medical Chemistry, Faculty of Medicine, University of Debrecen, Debrecen, Hungary
[5]HUN-REN-DE Cell Biology and Signaling Research Group, Debrecen, Hungary
[6]Department of Pharmaceutical Biotechnology, Faculty of Pharmacy, University of Pécs, Pécs, Hungary
[7]Department of Pathology, Faculty of Medicine, University of Debrecen, Debrecen, Hungary
[8]Department of Biochemistry and Molecular Biology, Faculty of Medicine, University of Debrecen, Debrecen, Hungary
[9]Department of Biochemistry, Institute of Chemistry, University of São Paulo, São Paulo, Brazil
[10]Medicinal Chemistry Research Group, Research Centre for Natural Sciences, Budapest, Hungary
[11]Department of Inorganic and Analytical Chemistry, Faculty of Chemical Technology and Biotechnology, Budapest University of Technology and Economics, Budapest, Hungary
[12]Department of Pharmacology and Pharmacotherapy, Medical School & Centre for Neuroscience, University of Pécs, Pécs, Hungary
[13]Department of Medical Biology, Medical School, Pécs, Hungary
[14]Department of Organic Chemistry, Faculty of Science and Technology, University of Debrecen, Debrecen, Hungary
[15]Doctoral School of Molecular Medicine, Semmelweis University, Budapest, Hungary
[16]Institute of Enzymology, Research Centre for Natural Sciences, Budapest, Hungary
[17]Department of Organic Chemistry and Technology, Faculty of Chemical Technology and Biotechnology, Budapest University of Technology and Economics, Budapest, Hungary
[18]Erzsébet Hospital, Sátoraljaújhely, Hungary
[19]Translational and Clinical Research Institute, Newcastle University Centre for Cancer, Faculty of Medical Sciences, Newcastle University, Newcastle upon Tyne, UK
[20]Hungarian Research Network, Chronic Pain Research Group, University of Pécs, Pécs, Hungary
[21]National Laboratory for Drug Research and Development, Budapest, Hungary
[22]Section of Clinical Physiology, Department of Cardiology, University of Debrecen, Debrecen, Hungary
[23]MTA-DE Lendület Laboratory of Cellular Metabolism, Debrecen, Hungary
[24]Research Center for Molecular Medicine, Faculty of Medicine, University of Debrecen, Debrecen, Hungary

ACKNOWLEDGEMENTS

The work was supported by grants from the NKFIH (K132623, K142141, K135150, SNN135335, PD142301, FK146852, TKP2021-EGA-10, TKP-2021-EGA-13, TKP2021-EGA-19, TKP2021-EGA-20, TKP2021-NVA-07, RRF-2.3.1-21-2022-00010, FK146063, 2020-1.1.2-PIACI-KFI-2020-00039). The Projects no. TKP2021-EGA-10, TKP-2021-EGA-13, TKP2021-EGA-19 and TKP2021-EGA-20 were implemented with the support provided from the National Research, Development and Innovation Fund of Hungary, financed under the TKP2021-EGA funding scheme. Project no. TKP2021-NVA-07 has been implemented with the support provided from the National Research, Development and Innovation Fund of Hungary, financed under the TKP2021-NVA funding scheme. The POST-COVID2021-33 grant to PB was from the Hungarian Academy of Sciences. FAPESP grants 2018/18007-5 and 2020/05317-6 were to NH. The research was performed in collaboration with Cell and Tissue Culture Core Facility at the Szentagothai Research Centre of the University of Pecs. The work of D.B. and A.S. were supported by the Janos Bolyai Research Scholarship of the Hungarian Academy of Sciences and the UNKP- 21-5 New National Excellence Program of the Ministry for Innovation and Technology. Prepared with the professional support of the Doctoral Student Scholarship Program of the Co-operative Doctoral Program of the Ministry of Innovation and Technology financed from the National Research, Development and Innovation Fund (to OM). The authors are grateful to Dr. Balázs Sarkadi (Institute of Enzymology, Research Centre for Natural Sciences, Budapest, Hungary) for his support and the critical revision of the manuscript. This project received funding from the HUN-REN Hungarian Research Network. Supported by the University of Debrecen Program for Scientific Publication.

CONFLICT OF INTEREST STATEMENT

Rucaparib was a generous gift from Clovis Oncology (Boulder, CO, USA). Clovis did not influence the study design and the conclusions drawn. Dr. Curtin is an inventor on patents WO 2005/012305 A2 and WO/2006/033006 with royalties paid to CRUK and Newcastle University; she gives her royalty share to charity and took no royalty in relation to this study. Other authors declare no conflict of interest.

DATA AVAILABILITY STATEMENT

Primary data are available at https://figshare.com/s/6b25fd3d5de80ab3f51e (DOI: 10.6084/m9.figshare.19418957).

DECLARATION OF TRANSPARENCY AND SCIENTIFIC RIGOUR

This Declaration acknowledges that this paper adheres to the principles for transparent reporting and scientific rigour of preclinical research as stated in the *BJP* guidelines for Design and Analysis and Immunoblotting and Immunochemistry, and as recommended by funding agencies, publishers and other organizations engaged with supporting research.

ORCID

Dávid Bajusz https://orcid.org/0000-0003-4277-9481
László Petri https://orcid.org/0000-0001-9881-5096
Tibor Viktor Szalai https://orcid.org/0009-0000-4088-3117
Zsuzsanna Helyes https://orcid.org/0000-0003-2435-4367
György M. Keserű https://orcid.org/0000-0003-1039-7809
Péter Bai https://orcid.org/0000-0002-6191-6616

REFERENCES

Abouhashem, A. S., Singh, K., Azzazy, H. M. E., & Sen, C. K. (2020). Is low alveolar type II cell SOD3 in the lungs of elderly linked to the observed severity of COVID-19? *Antioxidants & Redox Signaling*, *33*(2), 59–65. https://doi.org/10.1089/ars.2020.8111

Alexander, S. P. H., Fabbro, D., Kelly, E., Mathie, A. A., Peters, J. A., Veale, E. L., Armstrong, J. F., Faccenda, E., Harding, S. D., Davies, J. A., Annett, S., Boison, D., Burns, K. E., Dessauer, C., Gertsch, J., Helsby, N. A., Izzo, A. A., Ostrom, R., Papapetropoulos, A., … Wong, S. S. (2023). The Concise Guide to PHARMACOLOGY 2023/24: Enzymes. *British Journal of Pharmacology*, *180*(Suppl 2), S289–S373. https://doi.org/10.1111/bph.16181

Alexander, S. P. H., Kelly, E., Mathie, A. A., Peters, J. A., Veale, E. L., Armstrong, J. F., Buneman, O. P., Faccenda, E., Harding, S. D., Spedding, M., Cidlowski, J. A., Fabbro, D., Davenport, A. P., Striessnig, J., Davies, J. A., Ahlers-Dannen, K. E., Alqinyah, M., Arumugam, T. V., Bodle, C., … Zolghadri, Y. (2023). The Concise Guide to PHARMACOLOGY 2023/24: Other Protein Targets. *British Journal of Pharmacology*, *180*, S1–S22. https://doi.org/10.1111/bph.16176

Alhammad, Y. M. O., Kashipathy, M. M., Roy, A., Gagné, J. P., McDonald, P., Gao, P., Nonfoux, L., Battaile, K. P., Johnson, D. K., Holmstrom, E. D., Poirier, G. G., Lovell, S., & Fehr, A. R. (2021). The SARS-CoV-2 conserved macrodomain is a mono-ADP-ribosylhydrolase. *Journal of Virology*, *95*(3), e01969–e01920. https://doi.org/10.1128/JVI.01969-20

Amanat, F., Stadlbauer, D., Strohmeier, S., Nguyen, T. H. O., Chromikova, V., McMahon, M., Jiang, K., Arunkumar, G. A., Jurczyszak, D., Polanco, J., Bermudez-Gonzalez, M., Kleiner, G., Aydillo, T., Miorin, L., Fierer, D. S., Lugo, L. A., Kojic, E. M., Stoever, J., Liu, S. T. H., … Krammer, F. (2020). A serological assay to detect SARS-CoV-2 seroconversion in humans. *Nature Medicine*, *26*(7), 1033–1036. https://doi.org/10.1038/s41591-020-0913-5

Antal, D., Pór, Á., Kovács, I., Dull, K., Póliska, S., Ujlaki, G., Demény, M. Á., Szöllősi, A. G., Kiss, B., Szegedi, A., Bai, P., & Szántó, M. (2023). PARP2 promotes inflammation in psoriasis by modulating estradiol biosynthesis in keratinocytes. *Journal of Molecular Medicine*, *101*(8), 987–999. https://doi.org/10.1007/s00109-023-02338-z

Bai, P., & Virag, L. (2012). Role of poly(ADP-ribose) polymerases in the regulation of inflammatory processes. *FEBS Letters*, *586*(21), 3771–3777. https://doi.org/10.1016/j.febslet.2012.09.026

Brenke, R., Kozakov, D., Chuang, G. Y., Beglov, D., Hall, D., Landon, M. R., Mattos, C., & Vajda, S. (2009). Fragment-based identification of druggable 'hot spots' of proteins using Fourier domain correlation techniques. *Bioinformatics*, *25*(5), 621–627. https://doi.org/10.1093/bioinformatics/btp036

Bustin, S. A., Benes, V., Garson, J. A., Hellemans, J., Huggett, J., Kubista, M., Mueller, R., Nolan, T., Pfaffl, M. W., Shipley, G. L., Vandesompele, J., & Wittwer, C. T. (2009). The MIQE guidelines: Minimum information for publication of quantitative real-time PCR experiments. *Clinical Chemistry*, *55*(4), 611–622. https://doi.org/10.1373/clinchem.2008.112797

Caprara, G., Prosperini, E., Piccolo, V., Sigismondo, G., Melacarne, A., Cuomo, A., Boothby, M., Rescigno, M., Bonaldi, T., & Natoli, G. (2018). PARP14 controls the nuclear accumulation of a subset of type I IFN-inducible proteins. *Journal of Immunology*, *200*(7), 2439–2454. https://doi.org/10.4049/jimmunol.1701117

Cossu, V., Bonanomi, M., Bauckneht, M., Ravera, S., Righi, N., Miceli, A., Morbelli, S., Orengo, A. M., Piccioli, P., Bruno, S., Gaglio, D., Sambuceti, G., & Marini, C. (2020). Two high-rate pentose-phosphate pathways in cancer cells. *Scientific Reports*, *10*(1), 22111. https://doi.org/10.1038/s41598-020-79185-2

Csonka, T., Murnyák, B., Szepesi, R., Kurucz, A., Klekner, Á., & Hortobágyi, T. (2014). Poly(ADP-ribose) polymerase-1 (PARP1) and p53 labelling index correlates with tumour grade in meningiomas. *Folia Neuropathologica*, *52*(2), 111–120. https://doi.org/10.5114/fn.2014.43782

Curtin, N., Bányai, K., Thaventhiran, J., le Quesne, J., Helyes, Z., & Bai, P. (2020). Repositioning PARP inhibitors for SARS-CoV-2 infection (COVID-19); a new multi-pronged therapy for acute respiratory distress syndrome? *British Journal of Pharmacology*, *177*(16), 3635–3645. https://doi.org/10.1111/bph.15137

Curtin, N. J., & Szabo, C. (2020). Poly(ADP-ribose) polymerase inhibition: Past, present and future. *Nature Reviews Drug Discovery*, *19*(10), 711–736. https://doi.org/10.1038/s41573-020-0076-6

Curtis, M.J., Alexander, S.P., Cirino, G., George, C.H., Kendall, D.A., Insel, P.A., Izzo, A.A., Ji, Y., Panettieri, R.A., Patel, H.H., Sobey, C.G., Stanford, S.C., Stanley, P., Stefanska, B., Stephens, G.J., Teixeira, M.M., Vergnolle, N., and Ahluwalia, A. (2022). Planning experiments: Updated guidance on experimental design and analysis and their reporting III. *Br J Pharmacol*; *179*:3907-3913. https://doi.org/10.1111/bph.15868.

Daugherty, M. D., Young, J. M., Kerns, J. A., & Malik, H. S. (2014). Rapid evolution of PARP genes suggests a broad role for ADP-ribosylation in host-virus conflicts. *PLoS Genetetics*, *10*(5), e1004403. https://doi.org/10.1371/journal.pgen.1004403

Drew, Y., Ledermann, J., Hall, G., Rea, D., Glasspool, R., Highley, M., Jayson, G., Sludden, J., Murray, J., Jamieson, D., Halford, S., Acton, G., Backholer, Z., Mangano, R., Boddy, A., Curtin, N., & Plummer, R. (2016). Phase 2 multicentre trial investigating intermittent and continuous dosing schedules of the poly(ADP-ribose) polymerase inhibitor rucaparib in germline BRCA mutation carriers with advanced ovarian and breast cancer. *British Journal of Cancer*, *114*(7), 723–730. https://doi.org/10.1038/bjc.2016.41

Fehr, A. R., Singh, S. A., Kerr, C. M., Mukai, S., Higashi, H., & Aikawa, M. (2020). The impact of PARPs and ADP-ribosylation on inflammation and host-pathogen interactions. *Genes and Development*, *34*(5–6), 341–359. https://doi.org/10.1101/gad.334425.119

Fodor, A., Tiperciuc, B., Login, C., Orasan, O. H., Lazar, A. L., Buchman, C., Hanghicel, P., Sitar-Taut, A., Suharoschi, R., Vulturar, R., & Cozma, A. (2021). Endothelial dysfunction, inflammation, and oxidative stress in COVID-19-mechanisms and therapeutic targets. *Oxidative Medicine and Cellular Longevity*, *2021*, 8671713.

Foo, J., Bellot, G., Pervaiz, S., & Alonso, S. (2022). Mitochondria-mediated oxidative stress during viral infection. *Trends in Microbiology*, *30*(7), 679–692. https://doi.org/10.1016/j.tim.2021.12.011

Friesner, R. A., Banks, J. L., Murphy, R. B., Halgren, T. A., Klicic, J. J., Mainz, D. T., Repasky, M. P., Knoll, E. H., Shelley, M., Perry, J. K., Shaw, D. E., Francis, P., & Shenkin, P. S. (2004). Glide: A new approach for rapid, accurate docking and scoring. 1. Method and assessment of docking accuracy. *Journal of Medical Chemistry*, *47*(7), 1739–1749. https://doi.org/10.1021/jm0306430

Fu, Y., Cheng, Y., & Wu, Y. (2020). Understanding SARS-CoV-2-mediated inflammatory responses: From mechanisms to potential therapeutic tools. *Virologica Sinica*, *35*(3), 266–271. https://doi.org/10.1007/s12250-020-00207-4

Gorbalenya, A. E., Baker, S., Baric, R. S., de Groot, R., Drosten, C., Gulyaeva, A. A., Haagmans, B., Lauber, C., Leontovich, A. M., Neuman, B. W., & Penzar, D. (2020). The species severe acute respiratory syndrome-related coronavirus: Classifying 2019-nCoV and naming it SARS-CoV-2. *Nature Microbiology*, *5*(4), 536–544. https://doi.org/10.1038/s41564-020-0695-z

Guo, T., Zuo, Y., Qian, L., Liu, J., Yuan, Y., Xu, K., Miao, Y., Feng, Q., Chen, X., Jin, L., Zhang, L., Dong, C., Xiong, S., & Zheng, H. (2019). ADP-ribosyltransferase PARP11 modulates the interferon antiviral response by mono-ADP-ribosylating the ubiquitin E3 ligase β-TrCP. *Nature Microbiology*, *4*(11), 1872–1884. https://doi.org/10.1038/s41564-019-0428-3

Halgren, T. A., Murphy, R. B., Friesner, R. A., Beard, H. S., Frye, L. L., Pollard, W. T., & Banks, J. L. (2004). Glide: A new approach for rapid, accurate docking and scoring. 2. Enrichment factors in database screening. *Journal of Medical Chemistry*, *47*(7), 1750–1759. https://doi.org/10.1021/jm030644s

Han, P., Li, L., Liu, S., Wang, Q., Zhang, D., Xu, Z., Han, P., Li, X., Peng, Q., Su, C., Huang, B., Li, D., Zhang, R., Tian, M., Fu, L., Gao, Y., Zhao, X., Liu, K., Qi, J., … Wang, P. (2022). Receptor binding and complex structures of human ACE2 to spike RBD from omicron and delta SARS-CoV-2. *Cell*, *185*(4), 630–640.e10. https://doi.org/10.1016/j.cell.2022.01.001

Heer, C. D., Sanderson, D. J., Voth, L. S., Alhammad, Y. M. O., Schmidt, M. S., Trammell, S. A. J., Perlman, S., Cohen, M. S., Fehr, A. R., & Brenner, C. (2020). Coronavirus infection and PARP expression dysregulate the NAD metabolome: An actionable component of innate immunity. *Journal of Biological Chemistry*, *295*(52), 17986–17996. https://doi.org/10.1074/jbc.RA120.015138

Hoffmann, M., Kleine-Weber, H., Schroeder, S., Krüger, N., Herrler, T., Erichsen, S., Schiergens, T. S., Herrler, G., Wu, N. H., Nitsche, A., Müller, M. A., Drosten, C., & Pöhlmann, S. (2020). SARS-CoV-2 cell entry depends on ACE2 and TMPRSS2 and is blocked by a clinically proven protease inhibitor. *Cell*, *181*(2), 271–280. https://doi.org/10.1016/j.cell.2020.02.052

Hwang, T. L., & Shaka, A. J. (1995). Water suppression that works. Excitation sculpting using arbitrary wave-forms and pulsed-field gradients. *Journal of Magnetic Resonance, Series a*, *112*(2), 275–279. https://doi.org/10.1006/jmra.1995.1047

Jia, K., & Jernigan, R. L. (2021). New amino acid substitution matrix brings sequence alignments into agreement with structure matches. *Proteins: Structure, Function, and Bioinformatics*, *89*(6), 671–682. https://doi.org/10.1002/prot.26050

Karu, N., Kindt, A., van Gammeren, A. J., Ermens, A. A. M., Harms, A. C., Portengen, L., Vermeulen, R. C. H., Dik, W. A., Langerak, A. W., van der Velden, V. H. J., & Hankemeier, T. (2022). Severe COVID-19 is characterised by perturbations in plasma amines correlated with immune response markers, and linked to inflammation and oxidative stress. *Metabolites*, *12*(7), 618. https://doi.org/10.3390/metabo12070618

Knezevic, C. E., Wright, G., Remsing Rix, L. L., Kim, W., Kuenzi, B. M., Luo, Y., Watters, J. M., Koomen, J. M., Haura, E. B., Monteiro, A. N., Radu, C., Lawrence, H. R., & Rix, U. (2016). Proteome-wide profiling of clinical PARP inhibitors reveals compound-specific secondary targets. *Cell Chemical Biology*, *23*(12), 1490–1503. https://doi.org/10.1016/j.chembiol.2016.10.011

Korber, B., Fischer, W. M., Gnanakaran, S., Yoon, H., Theiler, J., Abfalterer, W., Hengartner, N., Giorgi, E. E., Bhattacharya, T., Foley, B., Hastie, K. M., Parker, M. D., Partridge, D. G., Evans, C. M., Freeman, T. M., de Silva, T. I., McDanal, C., Perez, L. G., Tang, H., … Wyles, M. D. (2020). Tracking changes in SARS-CoV-2 spike: Evidence that D614G increases infectivity of the COVID-19 virus. *Cell*, *182*(4), 812–827.e19. https://doi.org/10.1016/j.cell.2020.06.043

Kövér, K. E., Groves, P., Jiménez-Barbero, J., & Batta, G. (2007). Molecular recognition and screening using a 15N group selective STD NMR method. *Journal of the American Chemical Society*, *129*(37), 11579–11582. https://doi.org/10.1021/ja073291l

Kozakov, D., Grove, L. E., Hall, D. R., Bohnuud, T., Mottarella, S. E., Luo, L., Xia, B., Beglov, D., & Vajda, S. (2015). The FTMap family of web servers for determining and characterizing ligand-binding hot spots of proteins. *Nature Protocols*, *10*(5), 733–755. https://doi.org/10.1038/nprot.2015.043

Kumar, N., AbdulRahman, A. K., AlAwadhi, A. I., & AlQahtani, M. (2021). Is glucose-6-phosphatase dehydrogenase deficiency associated with severe outcomes in hospitalized COVID-19 patients? *Scientific Reports*, *11*(1), 19213. https://doi.org/10.1038/s41598-021-98712-3

LaFargue, C. J., Dal Molin, G. Z., Sood, A. K., & Coleman, R. L. (2019). Exploring and comparing adverse events between PARP inhibitors. *Lancet Oncology*, *20*(1), e15–e28. https://doi.org/10.1016/S1470-2045(18)30786-1

Lan, J., Ge, J., Yu, J., Shan, S., Zhou, H., Fan, S., Zhang, Q., Shi, X., Wang, Q., Zhang, L., & Wang, X. (2020). Structure of the SARS-CoV-2 spike receptor-binding domain bound to the ACE2 receptor. *Nature*, *581*(7807), 215–220. https://doi.org/10.1038/s41586-020-2180-5

Liontos, M., Terpos, E., Markellos, C., Zagouri, F., Briasoulis, A., Katsiana, I., Skafida, E., Fiste, O., Kunadis, E., Andrikopoulou, A., Kaparelou, M., Koutsoukos, K., Gavriatopoulou, M., Kastritis, E., Trougakos, I. P., & Dimopoulos, M. A. (2021). Immunological response to COVID-19 vaccination in ovarian cancer patients receiving PARP inhibitors. *Vaccines (Basel)*, *9*(10), 1148. https://doi.org/10.3390/vaccines9101148

Lüscher, B., Ahel, I., Altmeyer, M., Ashworth, A., Bai, P., Chang, P., Cohen, M., Corda, D., Dantzer, F., Daugherty, M. D., Dawson, T. M., Dawson, V. L., Deindl, S., Fehr, A. R., Feijs, K. L. H., Filippov, D. V., Gagné, J. P., Grimaldi, G., Guettler, S., … Ziegler, M. (2022). ADP-ribosyltransferases, an update on function and nomenclature. *FEBS Journal*, *289*(23), 7399–7410. https://doi.org/10.1111/febs.16142

Mahdi, M., Szojka, Z., Mótyán, J. A., & Tőzsér, J. (2018). Inhibitory effects of HIV-2 Vpx on replication of HIV-1. *Journal of Virology*, *92*(14), e00554–e00518. https://doi.org/10.1128/JVI.00554-18

Mayer, M., & Meyer, B. (2001). Group epitope mapping by saturation transfer difference NMR to identify segments of a ligand in direct contact with a protein receptor. *Journal of the American Chemical Society*, *123*(25), 6108–6117.

McElvaney, O. J., McEvoy, N. L., McElvaney, O. F., Carroll, T. P., Murphy, M. P., Dunlea, D. M., Ní Choileáin, O., Clarke, J., O'Connor, E.,

Hogan, G., Ryan, D., Sulaiman, I., Gunaratnam, C., Branagan, P., O'Brien, M. E., Morgan, R. K., Costello, R. W., Hurley, K., Walsh, S., … McElvaney, N. G. (2020). Characterization of the inflammatory response to severe COVID-19 illness. *American Journal of Respiratory and Critical Care Medicine*, *202*(6), 812–821. https://doi.org/10.1164/rccm.202005-1583OC

Meyer, B., Weimar, T., & Peters, T. (1997). Screening mixtures for biological activity by NMR. *European Journal of Biochemistry*, *246*(3), 705–709. https://doi.org/10.1111/j.1432-1033.1997.t01-1-00705.x

Montiel, V., Lobysheva, I., Gérard, L., Vermeersch, M., Perez-Morga, D., Castelein, T., Mesland, J. B., Hantson, P., Collienne, C., Gruson, D., van Dievoet, M. A., Persu, A., Beauloye, C., Dechamps, M., Belkhir, L., Robert, A., Derive, M., Laterre, P. F., Danser, A. H. J., … Balligand, J. L. (2022). Oxidative stress-induced endothelial dysfunction and decreased vascular nitric oxide in COVID-19 patients. *eBioMedicine*, *77*, 103893. https://doi.org/10.1016/j.ebiom.2022.103893

Morrow, D. A., Brickman, C. M., Murphy, S. A., Baran, K., Krakover, R., Dauerman, H., Kumar, S., Slomowitz, N., Grip, L., McCabe, C., & Salzman, A. L. (2009). A randomized, placebo-controlled trial to evaluate the tolerability, safety, pharmacokinetics, and pharmacodynamics of a potent inhibitor of poly(ADP-ribose) polymerase (INO-1001) in patients with ST-elevation myocardial infarction undergoing primary percutaneous coronary intervention: Results of the TIMI 37 trial. *Journal of Thrombosis and Thrombolysis*, *27*(4), 359–364. https://doi.org/10.1007/s11239-008-0230-1

Murray, J., Thomas, H., Berry, P., Kyle, S., Patterson, M., Jones, C., Los, G., Hostomsky, Z., Plummer, E. R., Boddy, A. V., & Curtin, N. J. (2014). Tumour cell retention of rucaparib, sustained PARP inhibition and efficacy of weekly as well as daily schedules. *British Journal of Cancer*, *110*(8), 1977–1984. https://doi.org/10.1038/bjc.2014.91

Oliver, F. J., Ménissier-de Murcia, J., Nacci, C., Decker, P., Andriantsitohaina, R., Muller, S., de la Rubia, G., Stoclet, J. C., & de Murcia, G. (1999). Resistance to endotoxic shock as a consequence of defective NF-κB activation in poly(ADP-ribose) polymerase-1 deficient mice. *EMBO Journal*, *18*(16), 4446–4454. https://doi.org/10.1093/emboj/18.16.4446

Pearson, W. R. (2013). Selecting the right similarity-scoring matrix. *Current Protocols in Bioinformatics*, *43*, 3.5.1–3.5.9. https://doi.org/10.1002/0471250953.bi0305s43

Piotto, M., Saudek, V., & Sklenář, V. (1992). Gradient-tailored excitation for single-quantum NMR spectroscopy of aqueous solutions. *Journal of Biomolecular NMR*, *2*(6), 661–665. https://doi.org/10.1007/BF02192855

Russo, L. C., Tomasin, R., Matos, I. A., Manucci, A. C., Sowa, S. T., Dale, K., Caldecott, K. W., Lehtiö, L., Schechtman, D., Meotti, F. C., Bruni-Cardoso, A., & Hoch, N. C. (2021). The SARS-CoV-2 Nsp3 macrodomain reverses PARP9/DTX3L-dependent ADP-ribosylation induced by interferon signaling. *Journal of Biological Chemistry*, *297*(3), 101041. https://doi.org/10.1016/j.jbc.2021.101041

Sastry, G. M., Adzhigirey, M., Day, T., Annabhimoju, R., & Sherman, W. (2013). Protein and ligand preparation: Parameters, protocols, and influence on virtual screening enrichments. *Journal of Computer-Aided Molecular Design*, *27*(3), 221–234. https://doi.org/10.1007/s10822-013-9644-8

Senesi, S., Csala, M., Marcolongo, P., Fulceri, R., Mandl, J., Banhegyi, G., & Benedetti, A. (2010). Hexose-6-phosphate dehydrogenase in the endoplasmic reticulum. *Biological Chemistry*, *391*(1), 1–8. https://doi.org/10.1515/bc.2009.146

Shapiro, G. I., Kristeleit, R. S., Burris, H. A., LoRusso, P., Patel, M. R., Drew, Y., Giordano, H., Maloney, L., Watkins, S., Goble, S., Jaw-Tsai, S., & Xiao, J. J. (2019). Pharmacokinetic study of rucaparib in patients with advanced solid tumors. *Clinical Pharmacology in Drug Development*, *8*(1), 107–118. https://doi.org/10.1002/cpdd.575

Smith, H.L., Willmore, E., Mukhopadhyay, A., Drew, Y., & Curtin, N.J., (2022) Differences in durability of PARP inhibition by clinically approved PARP inhibitors: implications for combinations and scheduling. bioRxiv, p. 2022.01.24.477471.

Tangos, M., Budde, H., Kolijn, D., Sieme, M., Zhazykbayeva, S., Lódi, M., Herwig, M., Gömöri, K., Hassoun, R., Robinson, E. L., Meister, T. L., Jaquet, K., Kovács, Á., Mustroph, J., Evert, K., Babel, N., Fagyas, M., Lindner, D., Püschel, K., … Hamdani, N. (2022). SARS-CoV-2 infects human cardiac myocytes promoted by inflammation and oxidative stress. *International Journal of Cardiology*, *362*, 196–205. https://doi.org/10.1016/j.ijcard.2022.05.055

Tauber, A. L., Schweiker, S. S., & Levonis, S. M. (2021). The potential association between PARP14 and SARS-CoV-2 infection (COVID-19). *Future Medicinal Chemistry*, *13*(6), 587–592. https://doi.org/10.4155/fmc-2020-0226

Unione, L., Moure, M. J., Lenza, M. P., Oyenarte, I., Ereño-Orbea, J., Ardá, A., & Jiménez-Barbero, J. (2022). The SARS-CoV-2 spike glycoprotein directly binds exogeneous sialic acids: A NMR view. *Angewandte Chemie International Edition*, *61*(18), e202201432. https://doi.org/10.1002/anie.202201432

Viegas, A., Manso, J., Nobrega, F. L., & Cabrita, E. J. (2011). Saturation-transfer difference (STD) NMR: A simple and fast method for ligand screening and characterization of protein binding. *Journal of Chemical Education*, *88*(7), 990–994. https://doi.org/10.1021/ed101169t

VTML200 amino acid homology matrix. 2023 [2023. 03. 28]; Available from: http://www.drive5.com/pop/VTML200I.

Waelchli, R., Bollbuck, B., Bruns, C., Buhl, T., Eder, J., Feifel, R., Hersperger, R., Janser, P., Revesz, L., Zerwes, H. G., & Schlapbach, A. (2006). Design and preparation of 2-benzamido-pyrimidines as inhibitors of IKK. *Bioorganic & Medicinal Chemistry Letters*, *16*(1), 108–112. https://doi.org/10.1016/j.bmcl.2005.09.035

Wagner, J., DuPont, A., Larson, S., Cash, B., & Farooq, A. (2020). Absolute lymphocyte count is a prognostic marker in Covid-19: A retrospective cohort review. *International Journal of Laboratory Hematology*, *42*(6), 761–765. https://doi.org/10.1111/ijlh.13288

Wahlberg, E., Karlberg, T., Kouznetsova, E., Markova, N., Macchiarulo, A., Thorsell, A. G., Pol, E., Frostell, Å., Ekblad, T., Öncü, D., Kull, B., Robertson, G. M., Pellicciari, R., Schüler, H., & Weigelt, J. (2012). Family-wide chemical profiling and structural analysis of PARP and tankyrase inhibitors. *Nature Biotechnology*, *30*(3), 283–288. https://doi.org/10.1038/nbt.2121

Wilson, R. H., Evans, T. R. J., Middleton, M. R., Molife, L. R., Spicer, J., Dieras, V., Roxburgh, P., Giordano, H., Jaw-Tsai, S., Goble, S., & Plummer, R. (2017). A phase I study of intravenous and oral rucaparib in combination with chemotherapy in patients with advanced solid tumours. *British Journal of Cancer*, *116*(7), 884–892. https://doi.org/10.1038/bjc.2017.36

Xing, J., Zhang, A., du, Y., Fang, M., Minze, L. J., Liu, Y. J., Li, X. C., & Zhang, Z. (2021). Identification of poly(ADP-ribose) polymerase 9 (PARP9) as a noncanonical sensor for RNA virus in dendritic cells. *Nature Communications*, *12*(1), 2681. https://doi.org/10.1038/s41467-021-23003-4

Zarn, K. E., Jaramillo, S. A., Zapata, A. R., Stone, N. E., Jones, A. N., Nunnally, H. E., Settles, E. W., Ng, K., Keim, P. S., Knudsen, S., Nuijten, P. M., Tijsma, A. S. L., & French, C. T. (2022). Stenoparib, an inhibitor of cellular poly(ADP-ribose) polymerases (PARPs), blocks in vitro replication of SARS-CoV-2 variants. *PLoS ONE*, *17*(9), e0272916. https://doi.org/10.1371/journal.pone.0272916

Zhu, N., Zhang, D., Wang, W., Li, X., Yang, B., Song, J., Zhao, X., Huang, B., Shi, W., Lu, R., Niu, P., Zhan, F., Ma, X., Wang, D., Xu, W., Wu, G., Gao, G. F., Tan, W., & China Novel Coronavirus Investigating and Research Team. (2020). A novel coronavirus from patients with pneumonia in China, 2019. *New England Journal of Medicine*, *382*(8), 727–733. https://doi.org/10.1056/NEJMoa2001017

SUPPORTING INFORMATION

Additional supporting information can be found online in the Supporting Information section at the end of this article.

How to cite this article: Papp, H., Tóth, E., Bóvári-Biri, J., Bánfai, K., Juhász, P., Mahdi, M., Russo, L. C., Bajusz, D., Sipos, A., Petri, L., Szalai, T. V., Kemény, Á., Madai, M., Kuczmog, A., Batta, G., Mózner, O., Vaskó, D., Hirsch, E., Bohus, P., … Bai, P. (2024). The PARP inhibitor rucaparib blocks SARS-CoV-2 virus binding to cells and the immune reaction in models of COVID-19. *British Journal of Pharmacology*, *181*(23), 4782–4803. https://doi.org/10.1111/bph.17305